ANL-79-93

DR. 569

ANL-79-93

524
540
11/23/80

MASTER

MATERIALS TECHNOLOGY FOR COAL-CONVERSION PROCESSES

Eighteenth Quarterly Report

April—June 1979

U of C-AUA-USDOE

ARGONNE NATIONAL LABORATORY, ARGONNE, ILLINOIS

Prepared for the Office of Fossil Energy,
U. S. DEPARTMENT OF ENERGY
under Contract W-31-109-Eng-38

The facilities of Argonne National Laboratory are owned by the United States Government. Under the terms of a contract (W-31-109-Eng-38) among the U. S. Department of Energy, Argonne Universities Association and The University of Chicago, the University employs the staff and operates the Laboratory in accordance with policies and programs formulated, approved and reviewed by the Association.

MEMBERS OF ARGONNE UNIVERSITIES ASSOCIATION

The University of Arizona
Carnegie-Mellon University
Case Western Reserve University
The University of Chicago
University of Cincinnati
Illinois Institute of Technology
University of Illinois
Indiana University
The University of Iowa
Iowa State University
The University of Kansas
Kansas State University
Loyola University of Chicago
Marquette University
The University of Michigan
Michigan State University
University of Minnesota
University of Missouri
Northwestern University
University of Notre Dame
The Ohio State University
Ohio University
The Pennsylvania State University
Purdue University
Saint Louis University
Southern Illinois University
The University of Texas at Austin
Washington University
Wayne State University
The University of Wisconsin-Madison

Printed in the United States of America
Available from
National Technical Information Service
U. S. Department of Commerce
5285 Port Royal Road
Springfield, VA 22161

NTIS price codes
Printed copy: A04
Microfiche copy: A01

Distribution Categories:
Coal Conversion and Utilization:
Coal Gasification (UC-90c)
Direct Combustion of Coal (UC-90e)
Materials and Components (UC-90h)

ANL-79-93

ARGONNE NATIONAL LABORATORY
9700 South Cass Avenue
Argonne, Illinois 60439

MATERIALS TECHNOLOGY FOR COAL-CONVERSION PROCESSES

Eighteenth Quarterly Report
April—June 1979

W. A. Ellingson
Program Manager

Materials Science Division

November 1979

Most recent reports in this series

ANL-78-79	April—June 1978
ANL-79-2	July—September 1978
ANL-79-23	October—December 1978
ANL-79-56	January—March 1979

TABLE OF CONTENTS

	Page
HIGHLIGHTS	viii
FOREWORD	x
ABSTRACT	x
INTRODUCTION	xi
Task A -- Evaluation of Ceramic Refractories for Slagging Gasifiers	1
Task C -- Development and Application of Nondestructive Evaluation Methods for Coal-conversion Processes	11
1. Erosive-wear Detection and Monitoring	11
a. Evaporated Compound Semiconductor Transducers	11
b. Momentary Contact Techniques	11
2. Component Inspection	12
a. Acoustic Monitoring of Valves	12
Task D -- Corrosion Behavior of Materials in Coal-conversion Processes	20
1. Corrosion in Gasification Environments	20
a. Effect of Alloying Additions on the Corrosion Behavior of Type 310 Stainless Steel	20
2. Effect of Sulfation Accelerators and Corrosion Inhibitors on Materials in Fluidized-bed Combustion Systems	30
a. Introduction	30
b. Results	31
Task E -- Erosion Behavior of Materials in Coal-conversion Processes	45
Task F -- Component Performance and Failure Analysis	48
a. Westinghouse Waltz-Mill Cyclone Nozzle Failure	48
b. Morgantown Energy Technology Center External Cyclone Failure	48
REFERENCES	55

LIST OF FIGURES

No.	Title	Page
1.	Furnace Plenum Temperature and Midheight Brick Temperatures 12.7 mm (0.5 in.) from the Hot Face of Full-length Bricks During Test Run 11	5
2.	Midheight Brick Temperatures vs Distance from Hot Face, 370 h After Start of Test Run 11	6
3.	Cut Sections of the Full-length Refractories Exposed to Slag Attack in Test Run 11	8
4.	Schematic Diagram of Test Section	14
5.	Variation of Coal Slurry Leakage Rate with Differential Pressure for the 3.17-, 5.16-, and 6.35-mm Orifices	15
6.	Schematic Diagram of Passive Acoustic Data Acquisition System	15
7.	A Typical Acoustic Spectrum Obtained from a 20% Coal-slurry Flowing through a 6.35-mm Orifice	16
8.	Acoustic Signal Amplitude vs Leakage Rate for Higher Differential Pressure Ranges	16
9.	Probability Distribution Function of Flow-induced Signal Amplitude	17
10.	Spectral Distribution of Acoustic Signal Taken from Converging Orifices	18
11.	Spectral Distribution of Acoustic Signal Taken from Diverging Orifices	19
12.	Engineering Stress-Engineering Strain Behavior for Incoloy 800 in the As-received and Thermally Aged Conditions and After 1000-h Exposures to Complex Gas Mixtures at 982°C	23
13.	Engineering Stress-Engineering Strain Behavior for Type 310 Stainless Steel in the As-received and Thermally Aged Conditions and After 1000-h Exposures to Complex Gas Mixtures at 982°C	23
14.	Engineering Stress-Engineering Strain Behavior for Inconel 671 in the As-received and Thermally Aged Conditions and After 1000-h Exposures to Complex Gas Mixtures at 982°C	24
15.	Engineering Stress-Engineering Strain Behavior for U.S. Steel Alloy 18-18-2 in the As-received and Thermally Aged Conditions and After 1000-h Exposures to Complex Gas Mixtures at 982°C	24

LIST OF FIGURES (contd.)

No.	Title	Page
16.	Engineering Stress-Engineering Strain Behavior for Incoloy 800 in the As-received and Thermally Aged Conditions and After 1000-h Exposures to Complex Gas Mixtures at 871°C	25
17.	Engineering Stress-Engineering Strain Behavior for Type 310 Stainless Steel in the As-received and Thermally Aged Conditions and After 1000-h Exposures to Complex Gas Mixtures at 871°C	25
18.	Engineering Stress-Engineering Strain Behavior for Inconel 671 in the As-received and Thermally Aged Conditions and After 1000-h Exposures to Complex Gas Mixtures at 871°C	26
19.	Periodic Table Showing Elements Which Form Oxides and Sulfides of Greater Stability Than Chromium Oxide and Chromium Sulfide	27
20.	Weight Gain vs Time Curves for Commercial and Ti-modified Type 310 Stainless Steel After Exposure at 1000°C to a Mixed Gas Environment with $p_{O_2} = 5.7 \times 10^{-17}$ atm, $p_{S_2} = 9.9 \times 10^{-6}$ atm, and $a_c = 0.024$	28
21.	Weight Gain vs Time Curves for Commercial and Ti-modified Type 310 Stainless Steel After Exposure at 1000°C to a Mixed Gas Environment with $p_{O_2} = 3.4 \times 10^{-16}$ atm, $p_{S_2} = 1.3 \times 10^{-6}$ atm, and $a_c = 0.017$	28
22.	Weight Gain vs Time Curves for Commercial and Ti-modified Type 310 Stainless Steel After Exposure at 1000°C to a Mixed Gas Environment with $p_{O_2} = 1.9 \times 10^{-16}$ atm, $p_{S_2} = 5.2 \times 10^{-7}$ atm, and $a_c = 0.020$	29
23.	Weight Gain vs Time Curves for Commercial and Ti-modified Type 310 Stainless Steel After Exposure at 1000°C to a Mixed Gas Environment with $p_{O_2} = 1.2 \times 10^{-16}$ atm, $p_{S_2} = 1.6 \times 10^{-7}$ atm, and $a_c = 0.022$	29
24.	SEM Micrographs of Type 310 Stainless Steel and Incoloy 800 After a 100-h Exposure Inside the Fluidized Bed	37
25.	SEM Micrographs of Inconel 601 and RA333 After a 100-h Exposure Inside the Fluidized Bed	38
26.	SEM Micrographs of Fe-2-1/4Cr-1Mo Steel After a 100-h Exposure Inside the Fluidized Bed	39
27.	SEM Micrographs of Fe-9Cr-1Mo Steel After a 100-h Exposure Inside the Fluidized Bed	40

LIST OF FIGURES (contd.)

No.	Title	Page
28.	SEM Micrograph and X-ray Images for Fe, O, Cr, Ca, S, Si, and K from a Fe-2-1/4Cr-1Mo Steel Specimen Exposed for (a) 100 h at 925 K Inside the Fluidized Bed, and (b) 100 h at 873 K Inside the Fluidized Bed Containing 0.5 mol % NaCl	41
29.	SEM Micrograph and X-ray Images for O, Cr, Fe, Ca, and Si from a Fe-9Cr-1Mo Steel Specimen Exposed for (a) 100 h at 970 K Inside The Fluidized Bed, and (b) 100 h at 895 K Inside the Fluidized Bed Containing 0.5 mol % NaCl	43
30.	Optical Micorgraphs of Cross Sections of Corroded Specimens Showing Corrosion Scale, Internal Corrosion and Metal Matrix . . .	47
31.	Optical Photographs of the Failed Westinghouse Waltz-Mill Nozzle .	49
32.	Scanning Electron Micrographs of a Fracture Surface from the Failed Nozzle, (a) away from and (b) near the OD	50
33.	Schematic Flow Diagram of Morgantown Energy Technology Center Stirred-bed Gasification System	51
34.	Drawing of the METC Hastelloy X Cyclone	52
35.	Macrophotographs of METC Hastelloy X Cyclone	53
36.	SEM Micrographs of the Cyclone ID Surface Shown in Fig. 34	54

LIST OF TABLES

No.	Title	Page
I.	Composition of Slag (wt %) During Corrosion Test Run 11	2
II.	Relative Corrosion Resistance of Sintered and Chemically Bonded Refractories Exposed to a Basic Slag in Test Run 11	3
III.	Relative Corrosion Resistance of Fused-cast Refractories Exposed to a Basic Slag in Test Run 11	4
IV.	Composition of Steels Used in the Program	22
V.	Experimental Conditions and Types of Scale Observed on the Specimens After Exposure at 1000°C	22
VI.	Calcium-to-Sulfur Molar Ratios Required to Maintain 700 ppm SO_2 in the Dry Off-Gas	32
VII.	Average Values of the Thickness of Surface Scale and Internal Corrosive Penetration Measured in Air-cooled Corrosion Specimens for Run CT-1	33
VIII.	Average Values of the Thickness of Surface Scale and Internal Corrosive Penetration Measured in Air-cooled Corrosion Specimens for Run CT-2	34
IX.	Average Values of the Thickness of Surface Scale and Internal Corrosive Penetration Measured in Air-cooled Corrosion Specimens for Run CT-3	35
X.	Average Values of the Thickness of Surface Scale and Internal Corrosive Penetration Measured in Air-cooled Corrosion Specimens for Run CT-4	36
XI.	Corrosion Calibration Test Results	46

HIGHLIGHTS

Task A -- Evaluation of Ceramic Refractories for Slagging Gasifiers *(C. R. Kennedy, R. J. Fousek, and S. W. Kreis)*

The results from test run 11 have been compiled and analyzed. In this test, 11 different water-cooled refractories were exposed to a basic slag (B/A = 1.5) for 500 h at a furnace plenum temperature of 1500°C. The fused-cast chrome spinel (number 22) proved to be the most resistant to corrosion. As in tests with acidic slags, the importance of high chromia content and high density was demonstrated.

Task C -- Development and Application of Nondestructive Evaluation Methods for Coal-conversion Processes *(W.A. Ellingson, K.J. Reimann, C.A. Youngdahl and R.A. Roberts)*

An extensive literature search has been completed on high-temperature ultrasonic coupling methods. This review has shown that vacuum-evaporated transducers may be useful for erosion-monitoring applications, and that no long-term pressure-coupling studies (which are needed in our program) have been conducted to date.

The acoustic slurry-loop modification was completed and initial tests using a 20% coal-water slurry were conducted. Use of cylindrical orifices of 2.38 and 6.35 mm indicated that the majority of the flow-induced acoustic energy was below 65 kHz, in agreement with previous data on oil and non-aerated tap water obtained in other studies.

Task D.1 -- Corrosion in Gasification Environments *(K. Natesan)*

Uniaxial tensile data were generated for Incoloy 800, Type 310 stainless steel, Inconel 671, and U. S. Steel Alloy 18-18-2 after a 1000-h exposure to multicomponent gas mixtures that simulate a coal-gasification environment. The preexposure of the materials to complex gas mixtures resulted in a decrease in ultimate tensile strength with only minimal changes in the uniform strain.

Thermogravimetric studies were conducted to evaluate the effect of titanium addition to the Type 310 stainless steel base composition on the corrosion behavior. In all the experiments conducted at 1000°C and over a wide range of oxygen and sulfur partial pressures, the modified steel exhibited higher corrosion rates than the commercial steel.

Task D.2 -- Effect of Sulfation Accelerators and Corrosion Inhibitors on Materials in Fluidized-bed Combustion Systems *(O.K. Chopra)*

The corrosion behavior of several commercial iron- and nickel-base alloys has been evaluated after 100-h exposures in the bed and freeboard regions of an atmospheric-pressure fluidized-bed combustor. The influence of small additions of NaCl, $CaCl_2$, and Na_2CO_3 (i.e., sulfation accelerators or enhancement agents) to the limestone on the average thickness of the surface scale and internal corrosive penetration at temperatures between 800 and 1128 K was determined from metallographic evaluation of the specimens. The results showed that at ∿ 1118 K the addition of 0.3 mol % $CaCl_2$ to the fluidized bed had no effect on the corrosion behavior of the various materials; however, 0.5 mol % NaCl or 1.9 mol % Na_2CO_3 increased the corrosion rate of most of the materials. In general, the austenitic stainless steels and Haynes Alloy 188 exhibit better resistance to accelerated corrosion in the presence of salts than the high-nickel alloys. The air-cooled specimens located inside the fluidized bed and the corrosion coupons placed in the freeboard section of the combustor at temperatures between 800 and 1000 K showed very little corrosion, with the exception of Fe-2-1/4Cr-1Mo and Fe-9Cr-1Mo steels, which were oxidized. At these temperatures the addition of salt has no effect on the corrosion behavior of any of the materials.

Task E -- Erosion Behavior of Materials in Coal-conversion Processes *(J.Y. Park, S. Danyluk, and W.J. Shack)*

A 150-h corrosion calibration test on 1015 carbon steel, Type 304 stainless steel, Incoloy 800 and Stellite 6B specimens was performed in a simulated gasifier atmosphere. Material degradation due to corrosion was measured in terms of weight change, loss of substrate thickness, scale formation, and internal corrosion. By these criteria, Incoloy 800 was the most corrosion-resistant alloy tested, and 1015 carbon steel was the least corrosion-resistant.

Task F -- Component Performance and Failure Analysis *(S. Danyluk and G.M. Dragel)*

One component each from the Westinghouse Waltz-Mill Pilot Plant and the Morgantown Energy Technology Center Stirred-bed Gasification Plant were examined. A field visit was made to the Westinghouse Plant in Madison, PA to discuss materials problems and interaction between ANL and Westinghouse. Two failure-analysis reports have been written: "Transgranular Chloride-assisted and Intergranular Stress-corrosion Cracking of Type 304 Stainless Steel Pipes from the IGT Steam-Iron Pilot Plant: Failure Analysis Report" (ANL/MSD/FE-79-1) and "Examination of a 15.24-cm Ball Valve from the Morgantown Energy Technology Center SOA Lockhopper Valve Testing and Development Project: Failure Analysis Report" (ANL/MSD/FE-79-4).

MATERIALS TECHNOLOGY FOR COAL-CONVERSION PROCESSES:
EIGHTEENTH QUARTERLY REPORT
April-June 1979

FOREWORD

This broad-base materials engineering program, begun in 1974, includes studies on ceramic (refractory) and metallic materials presently being used or intended for use in coal-conversion processes. The program entails nondestructive testing, failure analysis, and studies of erosive wear, corrosion and refractory degradation. Appropriate laboratory and field experiments are integrated such that the results have impact on present pilot- and demonstration-plant and proposed full-scale designs. This quarterly report, for the period April-June 1979, presents the technical accomplishments of the program.

ABSTRACT

A 500-h test run, exposing 11 water-cooled refractories to basic slag (B/A = 1.5), was completed. High chromia content and high density again appeared to be significant factors contributing to the corrosion resistance of refractories used for slag containment.

A literature review on high-temperature ultrasonic coupling was completed and suggested that studies on long-term (months to years) pressure-coupling stability are needed. Flow-induced acoustic-energy studies (relevant to acoustic leak detection) suggested that a 20% coal-water slurry flowing through an orifice under pressure produces acoustic-energy excitation mainly at frequencies < 65 kHz, and that a better correlation between acoustic rms levels and flow rate is obtained as the differential pressure is increased.

Corrosion studies of Type 310 stainless steel at 1000°C with various P_{O_2} and P_{S_2} suggested that titanium addition increases the corrosion rate relative to that of commercially available steels. Fluid-bed corrosion studies showed that at temperatures of 800-1000 K addition of salt has no effect on the corrosion behavior of any material examined.

Failure analyses were performed on a cyclone nozzle from the Westinghouse Waltz-Mill combined cycle coal-gasification plant and an external cyclone from the Morgantown Energy Technology Center Stirred-bed Gasifier.

INTRODUCTION

The economical conversion of coal into clean and usable fuels will be advanced through the use of durable materials systems. The technical information base applicable to materials selection in plant design for the operating environments of various coal-conversion processes is extremely limited. Hence, reliable selection and lifetime-prediction methods for materials under these conditions are not available. This project is designed to provide part of the materials information necessary for successful operation of coal-conversion systems. The present report is the eighteenth quarterly progress report submitted by ANL to the Division of Systems Engineering, Office of Fossil Energy under Project Number 7106, "Materials Technology for Coal-conversion Processes".

The project includes six tasks: (A) Evaluation of commercial refractories exposed to coal slag under conditions typical of those encountered in slagging gasification processes; (B) evaluation of erosion/corrosion-resistant coatings when exposed to prototype operating environments (suspended in FY 79); (C) development, evaluation, and application of nondestructive evaluation methods applicable to coal-conversion systems; (D) evaluation of the corrosion behavior of commercial alloys; (E) development of analytical models to predict the erosive-wear behavior of materials used in coal-conversion plants; and (F) analysis of failed coal-conversion plant components.

Task A -- Evaluation of Ceramic Refractories for Slagging Gasifiers
(C. R. Kennedy, R. J. Pousek, and S. W. Kreis)

In test run 11, a variety of water-cooled refractories were exposed for 503 h at a furnace plenum temperature of 1500°C to a synthetic coal slag (Table I) with a base-to-acid ratio of 1.5. The partial pressure of oxygen was $\sim 10^{-3}$ Pa throughout the test, resulting in a ferritic content in the slag of ~26%. Half- and full-length (228 mm) bricks of each type were tested (with the exception of number 280, which was tested only full-length). Most of the bricks were instrumented with thermocouples; temperatures of several bricks during the test run are shown in Figs. 1 and 2 as a function of time and distance from the hot face, respectively. The hot-face temperature of refractory number 2, as measured by an optical pyrometer, was ~1430-1450°C throughout the test. The compositions and relative corrosion resistance of the refractories are presented in Tables II and III. Posttest photographs of cut sections of the full-length bricks are shown in Fig. 3.

As in tests with acidic slags, the effects of chromia content and density on corrosion resistance were evident. The most corrosion-resistant refractory was the fused-cast chrome-spinel (number 22). Even the half-length chrome-spinel brick, which was tested without water cooling, exhibited little attack. The fused-cast alumina-32% chromia refractory (number 280) also evinced excellent corrosion resistance, but was badly cracked (Fig. 3i) by thermal shock. As the chromia content was decreased, the resistance of alumina-chromia refractories to corrosive attack decreased rapidly. The alumina-10% chromia refractories (number 16, a sintered product, and number 86, a ramming mix) suffered only about the same amount of corrosion as did the fused-cast alumina refractory (number 2), despite much higher porosity (~17% for numbers 16 and 86 versus 1% for number 3). However, these lower-density products were penetrated to a much greater degree by the slag, resulting in substantial swelling above the slag line (see Figs. 3b and 3g).

The corrosion resistance of the three magnesia-chrome refractories was comparable to that of the alumina-16% chromia product (number 852), whereas the fused-cast magnesia-spinel was severely attacked.

Metallography and scanning electron microscopy to determine the degradation mechanisms in these refractories is currently in progress and will be presented in a future quarterly report.

TABLE I. Composition of Slag (wt %) During Corrosion Test Run 11

Component	Exposure Time, h[a]		
	1	303	398
SiO_2 (S)	25.1	23.0	25.1
Al_2O_3 (A)	15.3	16.1	15.0
Fe_2O_3 (F_1)	4.3	4.2	4.2
FeO (F_2)	8.3	9.4	9.2
Fe (F_3)	1.0	0.9	1.0
CaO (C)	39.2	39.4	38.2
MgO (M)	5.5	5.9	5.8
Na_2O (N)	<0.1	<0.1	<0.1
K_2O (K)	<0.1	<0.1	<0.1
TiO_2 (T)	1.0	1.0	1.1
B/A Ratio[b]	1.4	1.5	1.4
Ferritic Content,[c] %	29	26	26

[a]Measured after the 1500°C operating temperature was reached.

[b]Base-to-acid ratio $B/A = \frac{(F_1 + F_2 + F_3 + C + M + N + K)}{(S + A + T)}$.

[c]Ferritic content $= \frac{\text{wt \% } (Fe_2O_3)}{\text{wt \% } (Fe_2O_3) + 1.11 \text{ wt \% } (FeO) + 1.43 \text{ wt \% } (Fe)}$.

TABLE II. Relative Corrosion Resistance of Sintered and Chemically Bonded Refractories Exposed to a Basic Slag in Test Run 11

Number	Type	Composition, wt %	Maximum Depth of Removal,[a] mm		Maximum Depth of Penetration,[a] mm	
			Full-length	1/2-length	Full-length	1/2-length
16	Sintered alumina-chromia	Al_2O_3(89.7)-Cr_2O_3(10)	10	5	18	7
852	Sintered alumina-chromia	Al_2O_3(81.1)-Cr_2O_3(16.6)-P_2O_5(0.8)-SiO_2(0.5)-Fe_2O_3(0.5)-Na_2O(0.5)	3	3	8	5
190	Sintered alumina-chromia	Al_2O_3(92)-Cr_2O_3(7.5)-SiO_2(0.5)	21	9	31	18
86	Chemically bonded alumina-chromia	Al_2O_3(84.5)-Cr_2O_3(10.5)-SiO_2(0.2)	10	4	16	12
29	Sintered magnesia-chrome	MgO(63)-Cr_2O_3(18)-Fe_2O_3(12)-Al_2O_3(5)-SiO_2(1)-CaO(1)	4	3	14	10
35	Sintered magnesia-chrome	MgO(60)-Cr_2O_3(15.5)-Al_2O_3(15)-Fe_2O_3(7)-SiO_2(1.5)-CaO(1)	4	4	16	12
41	Sintered magnesia-chrome	MgO(55)-Cr_2O_3(20)-Al_2O_3(8)-FeO(11)-SiO_2(2.5)-CaO(0.5)-TiO_2(1.5)	5	4	20	10

[a]Measured from the original hot face.

TABLE III. Relative Corrosion Resistance of Fused-cast Refractories Exposed to a Basic Slag in Test Run 11

Number	Type	Composition, wt %	Maximum Depth of Removal,[a] mm		Maximum Depth of Penetration,[a] mm	
			Full-length	1/2-length	Full-length	1/2-length
2	Alumina	Al_2O_3(99)-Na_2O(0.5)	10	8	13	10
280	Alumina-chromia	Al_2O_3(65)-Cr_2O_3(32)-FeO(1)-CaO(0.6)-MgO(0.6)	1		1	NT
22	Chrome-spinel	Cr_2O_3(80)-MgO(8)-Fe_2O_3(6)-Al_2O_3(5)-SiO_2(1)	0-1	1[c]	2	2[c]
317	Magnesia-spinel	MgO(65)-Al_2O_3(35)	15	13	18	14

[a]Measured from the original hot face.

[b]NT = not tested.

[c]Without water cooling.

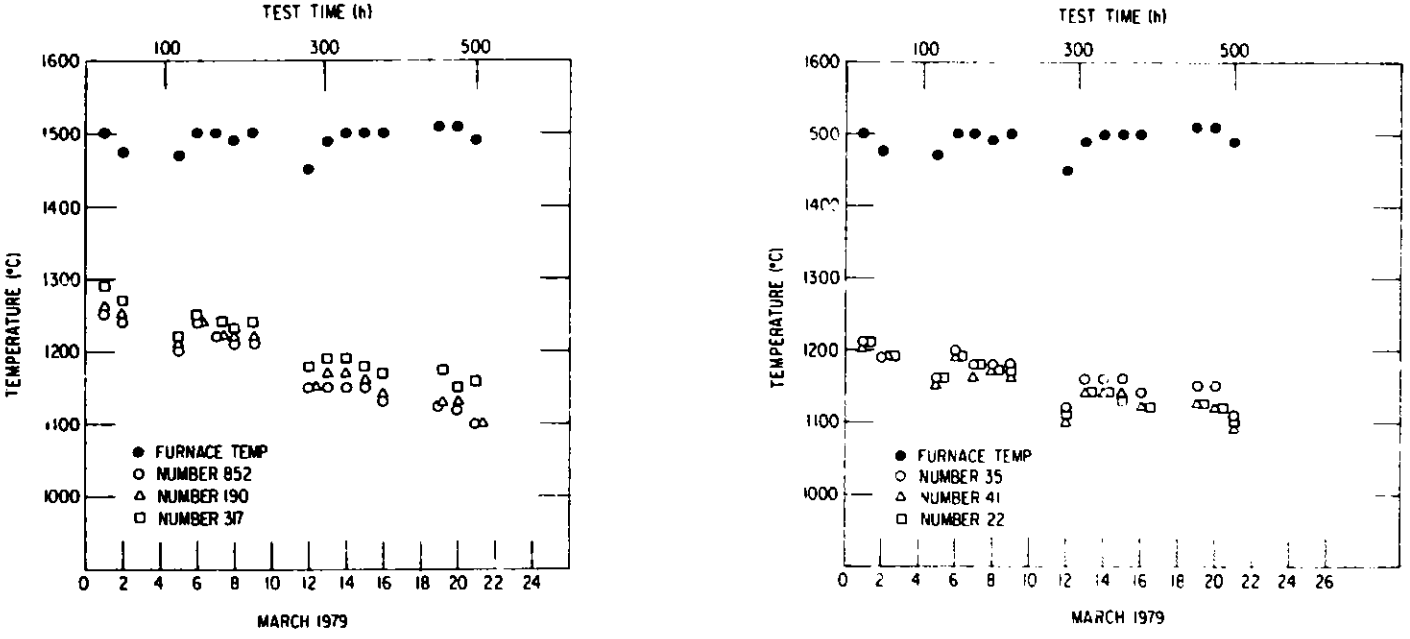

Fig. 1. Furnace Plenum Temperature and Midheight Brick Temperatures 12.7 mm (0.5 in.) from the Hot Face of Full-length Bricks During Test Run 11. ANL Neg. No. 306-79-863.

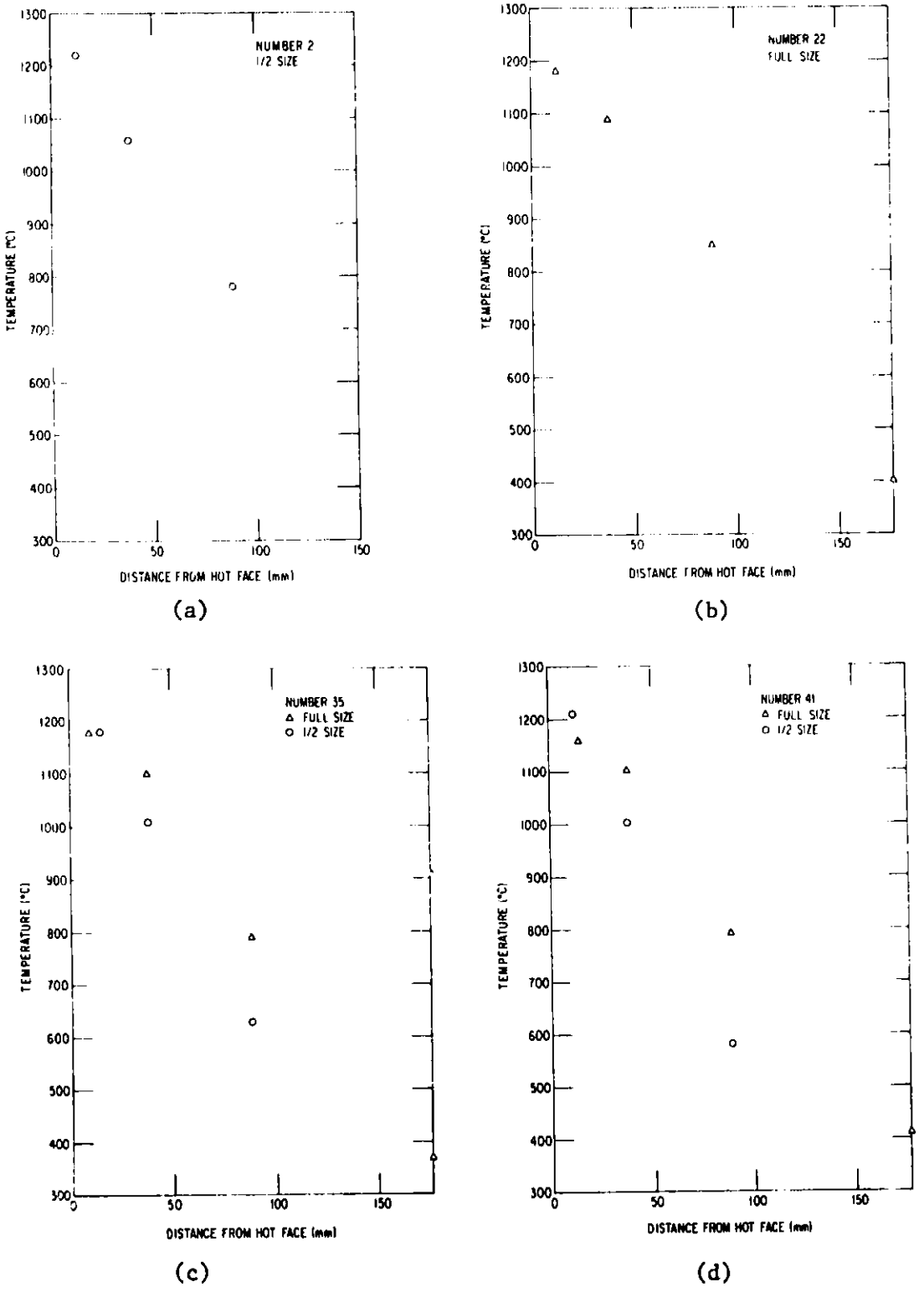

Fig. 2. Midheight Brick Temperatures vs Distance from Hot Face, 370 h After Start of Test Run 11. (a) Number 2, (b) number 22, (c) number 35, (d) Number 41, (e) number 86, (f) number 190, (g) number 317, and (h) number 852. ANL Neg. Nos. 306-79-868 and 865.

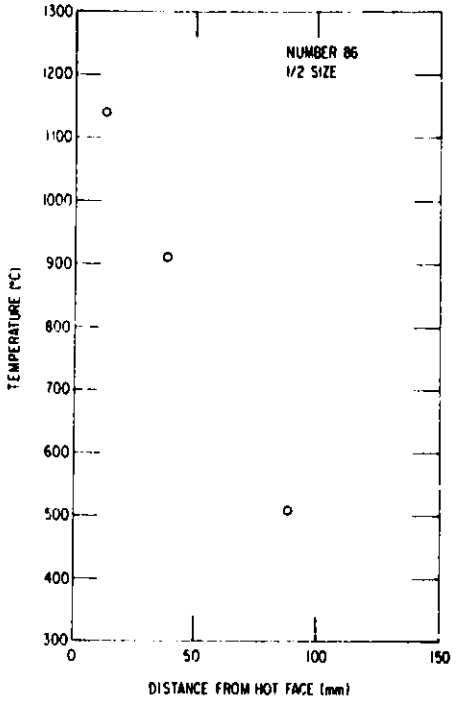

(e)

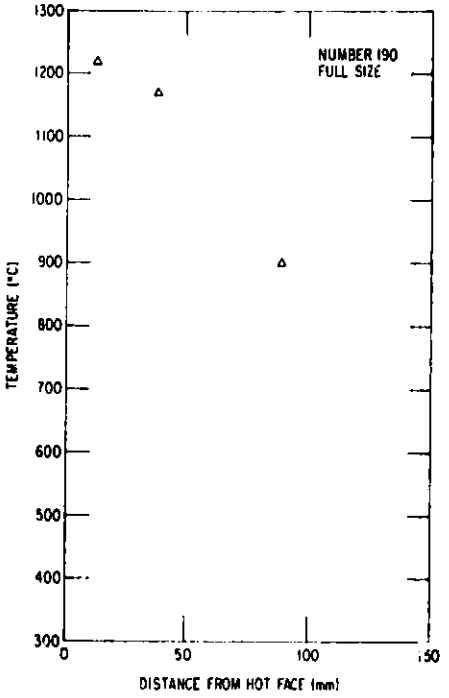

(f)

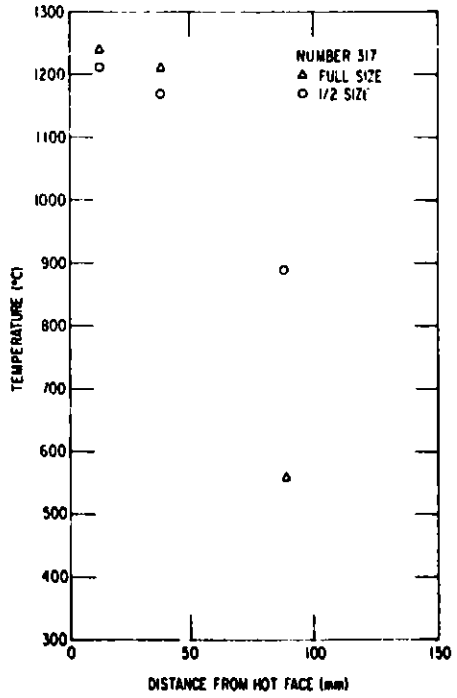

(g)

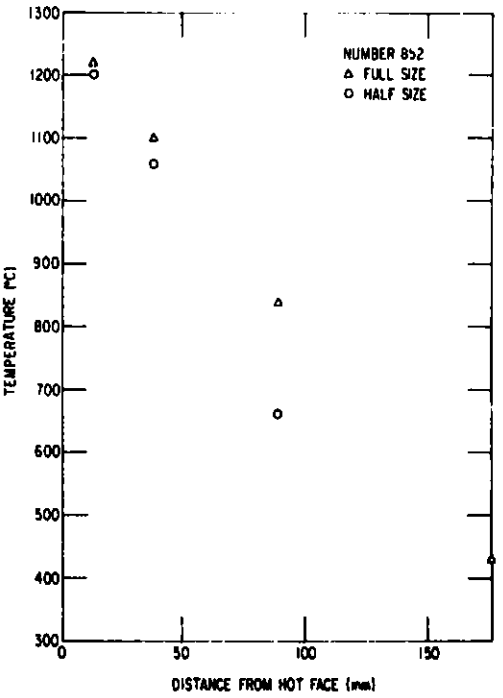

(h)

Fig. 2 (contd.)

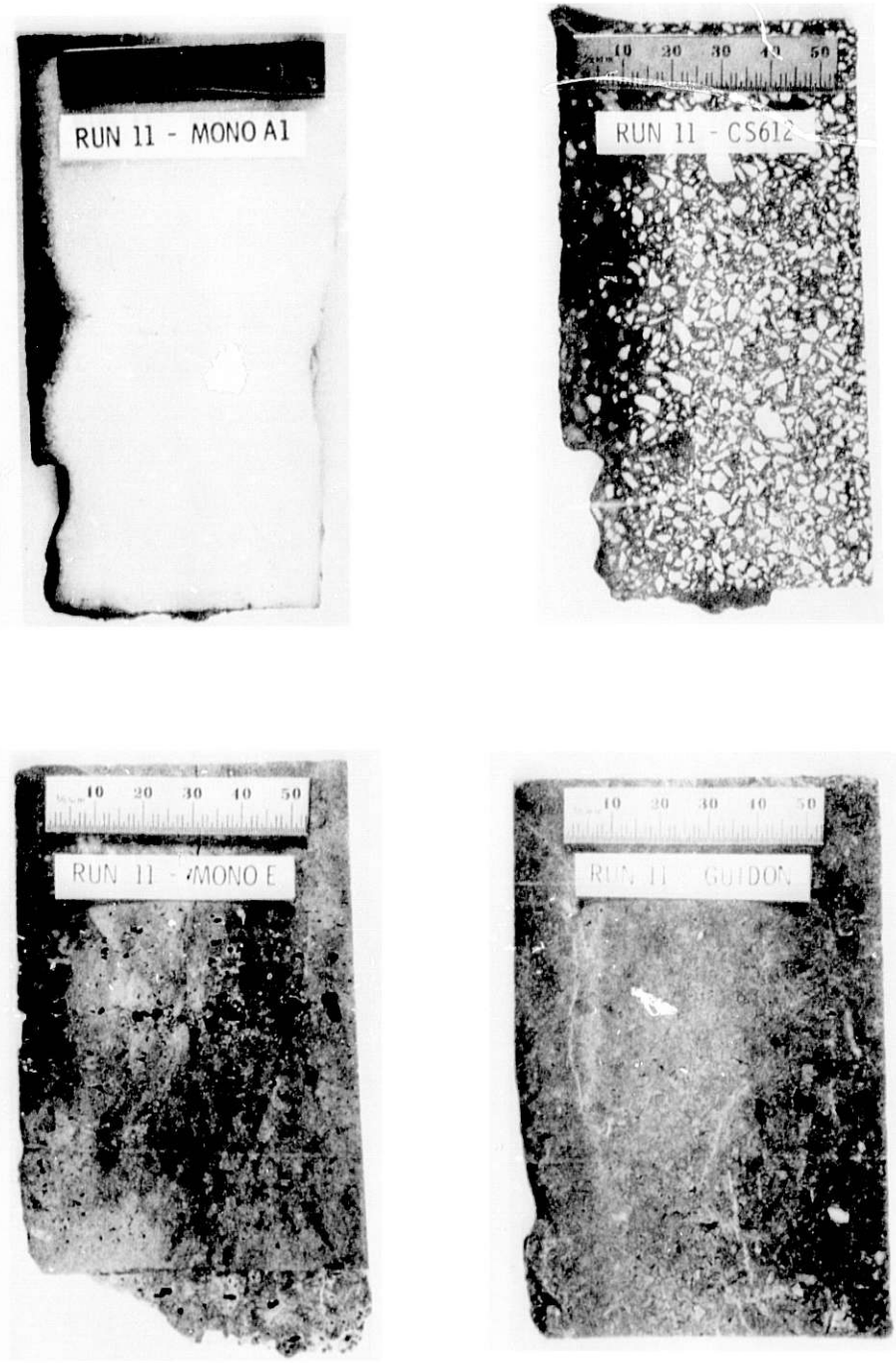

Fig. 3. Cut Sections of the Full-length Refractories Exposed to Slag Attack in Test Run 11. (a) Number 2, (b) number 16, (c) number 22, (d) number 29, (e) number 35, (f) number 41, (g) number 86, (h) number 90, (i) number 280, (j) number 37, and (k) number 852. The left-hand faces of (a)-(i) and (k) and the right-hand face of (j) were exposed to the slag. ANL Neg. Nos. 306-79-873, 874 and 872.

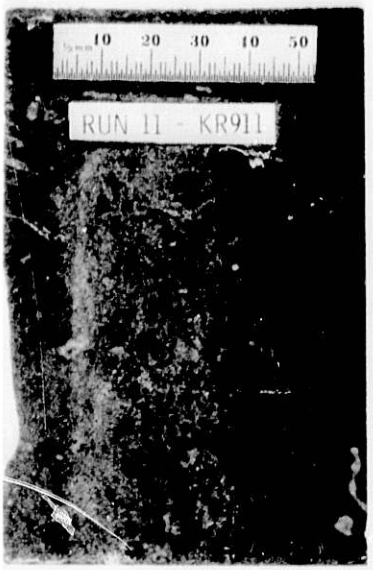

(e)

(f)

(g)

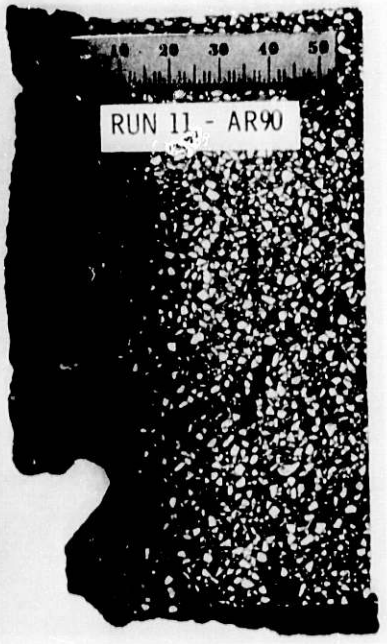

(h)

Fig. 3 (contd.)

(j)

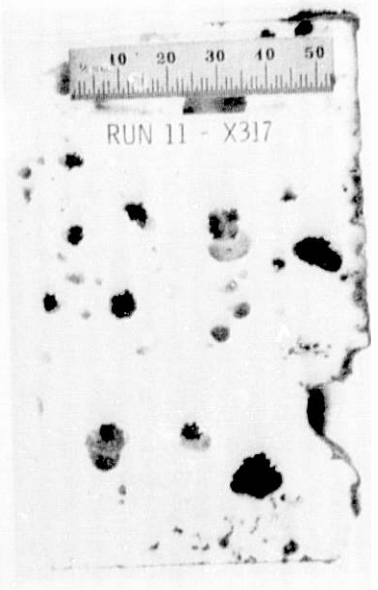

(k)

Fig. 3 (contd.)

Task C -- Development and Application of Nondestructive Evaluation Methods for Coal-conversion Processes *(W.A. Ellingson, K.J. Reimann, C.A. Youngdahl and R.A. Roberts)*

1. Erosive-wear Detection and Monitoring

An extensive review of high-temperature ultrasonic coupling methods was completed during the current quarter.[1] This project was undertaken because some applications will not allow use of the weld-coupling technique[2] which has been successfully developed. The following text discusses the significant findings of the review.

a. Evaporated Compound Semiconductor Transducers

Most of the groundwork for evaporated transducer production was done by Foster[3] at Bell Labs and Lord[4] at Brown (now Drexel). Transducer material, usually CdS, is vacuum-evaporated onto the surface of the item to be tested. The surface must be kept at temperatures in excess of 150° for the technique to work. The CdS condenses into a polycrystalline film with a strong preferred crystallographic orientation (the "C" axis normal to the surface). Experimental work has shown decaying echo patterns at frequencies above 20 MHz for temperatures to 600°C.

The technique has distinct potential for high-temperature applications if a high-frequency (20-100 MHz) acoustic wave is acceptable and enough acoustic power can be transmitted to the sample of interest. Nevertheless, we would need to initiate a development program to bring this methodology to a useful stage.

b. Momentary Contact Techniques

Lynnworth and Carnevale[5] of Panametrics reported successful use of a technique in which a transducer was pressed against a hot surface at pressures from a few thousand Pa to 206 MPa (30 ksi) for less than one second. The acoustic properties measured during this brief contact allowed measurement of the wall thickness of tubing and the position of the solid-liquid interface in a solidifying steel ingot. Surface temperatures were in excess of 700°C in many applications, and both shear and longitudinal waves were employed. The smoother the surface of the item to be probed, the lower the pressure required: Thus, rough (as-cast) surfaces required 206 MPa (30 ksi); machined surfaces required 6.9 MPa (1 ksi); and polished optical flats required only finger pressure.

Dr. N.O. Cross (EXXON)[6] has used greases of various viscosities, including a silicone grease, as coupling agents for momentary-contact measurements at relatively low temperatures. "Echo-Temp" grease has been used successfully at temperatures between 250 and 600°C. Dr. Richard Chaney (AMOCO)[7] has used Shell plastic strips for momentary-contact measurements at temperatures above 300°C. (These strips melt at 150-300°C).

Pressure coupling has been discussed by Krautkramer[8] and extensive experimental work has been done by Karplus et al. at Argonne.[9]

However, for monitoring erosive wear at high temperature, the stability of the pressure coupling is of importance and there appears to be no published work which addresses pressure-coupling stability for the time periods of interest here, namely months to years. The direction of the pressure-coupling program at ANL will be to discover suitable materials which are stable over long time spans.

2. Component Inspection

a. Acoustic Monitoring of Valves

Work continued this quarter on evaluating the potential use of passive acoustic techniques to detect internal leakage of coal-slurry valves. Last quarter[10] a brief description was given of an existing slurry-loop system which was to be modified to accept a new test section. This quarter the test section was built and installed, and tests were conducted. Figure 4 shows the 1.83-m (6-ft.) test section of 5-cm (2-in.) steel pipe with instrumentation and test orifice plate locations.

The initial run of the slurry loop revealed wildly fluctuating differential pressures due to pump surge. Accurate acoustic measurements were almost impossible because of the strong dependence of flow-induced acoustic levels on differential pressure. To reduce this problem, further modifications were made to the slurry loop. A 30-ℓ (8-gal) accumulator tank was added and a valve was replaced with a 1.5-m (5-ft.) vertical standpipe. These modifications, in conjunction with proper throttling of the flow, provided differential pressures at the orifice which varied by only ± 3.5 kPa (± 0.5 psi).

Flow rates were recorded for differential pressures ranging from 35 to 207 kPa (5 to 30 psi) in 17.5-kPa (2.5-psi) increments. A plot showing flow rate vs differential pressure for the 3.18-, 5.15-, and 6.35-mm (1/8-, 13/64-, and 1/4-in.) orifices is given in Fig. 5.

Four right circular orifices were to be tested to provide four points per differential pressure on a plot of detected acoustic amplitude vs leakage rate. However, the 2.38-mm (3/32-in.) orifice was extremely susceptible to plugging by compacting coal particles, which prevented the collection of data for this orifice. Because of the plugging of smaller orifices it was imposaible to determine a minimum detectable leakage rate. Up until the time the 2.38-mm orifice became plugged (about one minute flow time), an appreciable acoustic signal was received. Inclusion of an orifice larger than 6.35 mm (1/4 in.) was decided against as impractical and unrealistic.

A schematic of the instrumentation used to process the detected signal is shown in Fig. 6. The transducer used throughout this study was an Acoustic Emission Technology Model AC30L. The electrical response of the transducer to the acoustic emission signal was amplified 50 dB by an Ortec 9454 preamplifier, then fed into a Hewlett-Packard spectrum analyzer. Figure 7 shows a typical spectral distribution. This spectrum shows strong signals at 16, 25, 35, and 65 kHz. Signals below 15 kHz are basically background noise. Background noise above 15 kHz was found to be negligible.

The presence of signal peaks at or near the aforementioned four frequencies is a characteristic found in the spectra of all orifices investigated at all differential pressures. Acoustic amplitude was measured by centering first a 1-kHz and then a 10-kHz bandwidth filter at each center frequency and recording rms output. Data on acoustic amplitude vs differential pressure were collected for each frequency peak and each bandwidth filter. Data were summed over all frequencies to yield an accumulated rms signal output vs differential pressure for each bandwidth. A plot of accumulated rms signal output vs differential pressure obtained with a 10-kHz bandwidth filter is shown in Fig. 8.

These measurements were carried out using the spectrum analyzer in the manual-scan mode. In this mode the internal filter can be placed at a single center frequency rather than being repeatedly swept over the spectrum as in normal operation. The bandwidth selector is used to select either a 1- or a 10-kHz bandwidth. The signal present at the vertical output is directly proportional to the rms input signal falling within the bandpass of the filter. The system is calibrated for all gain settings using a sine-wave generator and a true rms voltmeter. The output voltage present at the vertical output was monitored by a Hewlett-Packard correlator operating in the probability density mode. The correlator directly provides the probability density function for continuously varying rms amplitude levels present at the vertical output. Figure 9 shows typical probability density functions taken from the correlator. The horizontal axis is rms voltage. The vertical axis represents the number of times the rms voltage measurement falls within a specific amplitude range. Each division on the horizontal scale is subdivided into 10 amplitude ranges. The horizontal scale is calibrated so that a full-scale deflection on the spectrum analyzer produces a full-scale deflection on the correlator. Full-scale vertical deflection on the correlator represents 65,536 measurements. Measurements are made at 0.1-ms intervals. The single peaked, symmetric distribution function shown in Fig. 9a suggests that flow-induced acoustic signals result from an ergodic process for a constant differential pressure.

Complete data (flow rate and acoustic signals) were taken for right circular orifices. The spectra of the tapered-bore orifices were examined for both converging and diverging configurations (see Figs. 10 and 11). These spectra show a marked similarity to the spectrum of the right circular orifices, suggesting that the spectral distribution function is relatively independent of the specific orifice geometry. In particular, note the near-identical positioning of the 25-, 32-, and 65-kHz peaks. These data support the feasibility of acoustically determining internal leakage with passive acoustic systems.

The work in this initial phase, although far from conclusive, does support the concept of passive acoustic detection of internal leakage in coal-slurry blockage valves at high differential pressures. In particular, it suggests physical conditions under which leakage could be monitored. However, the effects of two important physical parameters, sump storage pressure and downstream pressure (back pressure), could not be studied in the facility used in this work. Future work will simulate actual conditions as closely as possible to obtain conclusive results.

A shortcoming of the results to date is the absence of a minimum detectable leakage rate as the result of orifice plugging by compacted coal particles. To deal with this problem, future work will study various particle loadings in the slurry. This will provide information on the effect of particle loading on flow-induced acoustic signals, thus providing an indication of the accuracy of minimum detectable leak-rate data obtained with little or no particle loading. The data obtained with the converging and diverging orifices suggest that the spectral distribution of the flow-induced acoustic signals is relatively independent of the exact orifice geometry. Future work will determine the validity of this observation. Ultimately, the flow-induced acoustic signals from randomly shaped orifices, such as actual damaged valves, will be investigated.

A paper entitled "Development of a Non-invasive Acoustic Leak Detection System for Large High Pressure Gas Valves" was presented to the 25th International Instrumentation Symposium held at Anaheim, CA, May 7-10, 1979.

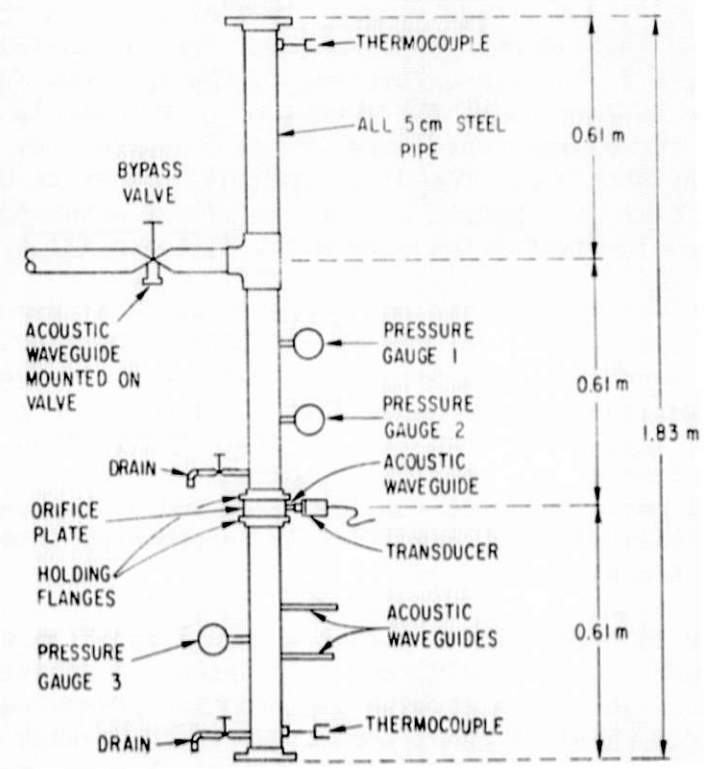

Fig. 4. Schematic Diagram of Test Section. Pressure gauges read 0 to 690 kPa. Drains are provided for changing orifice plates. ANL Neg. No. 306-79-896.

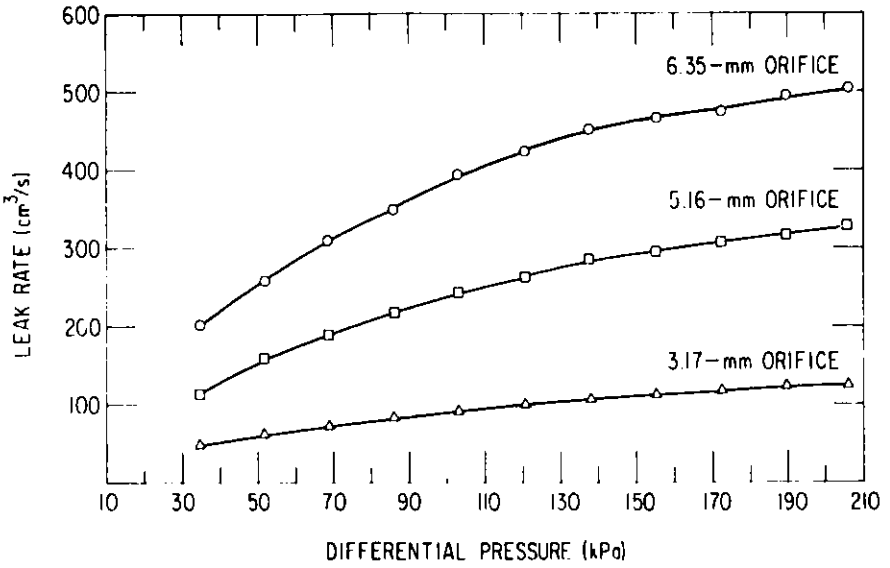

Fig. 5. Variation of Coal Slurry Leakage Rate with Differential Pressure for the 3.17-, 5.16-, and 6.35-mm Orifices. ANL Neg. No. 306-79-899.

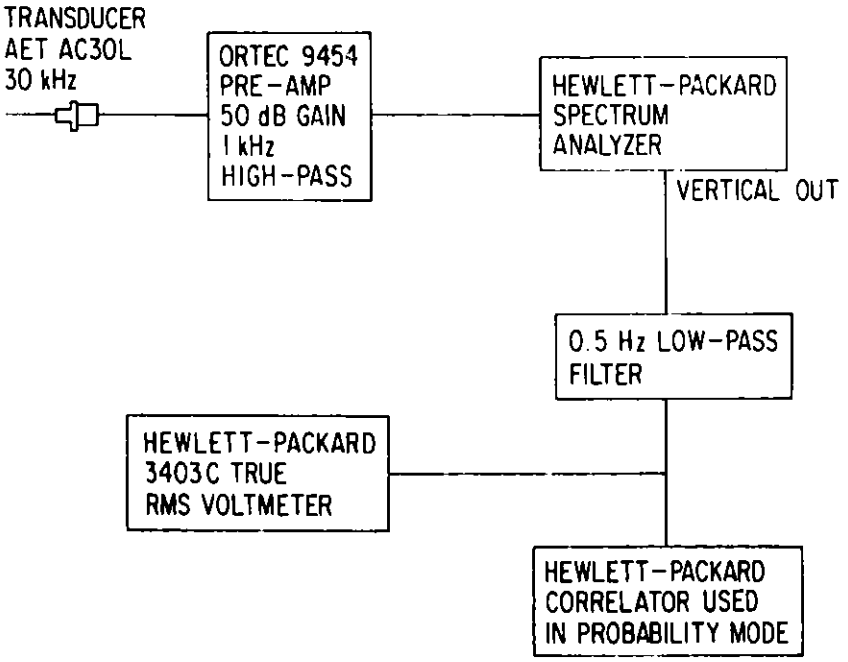

Fig. 6. Schematic Diagram of Passive Acoustic Data Acquisition System. Low-frequency noise is filtered at the preamplifier. The signal fed to the rms voltmeter and correlator is taken from the vertical output when the spectrum analyzer is used in the manual-scan mode. ANL Neg. No. 306-79-902.

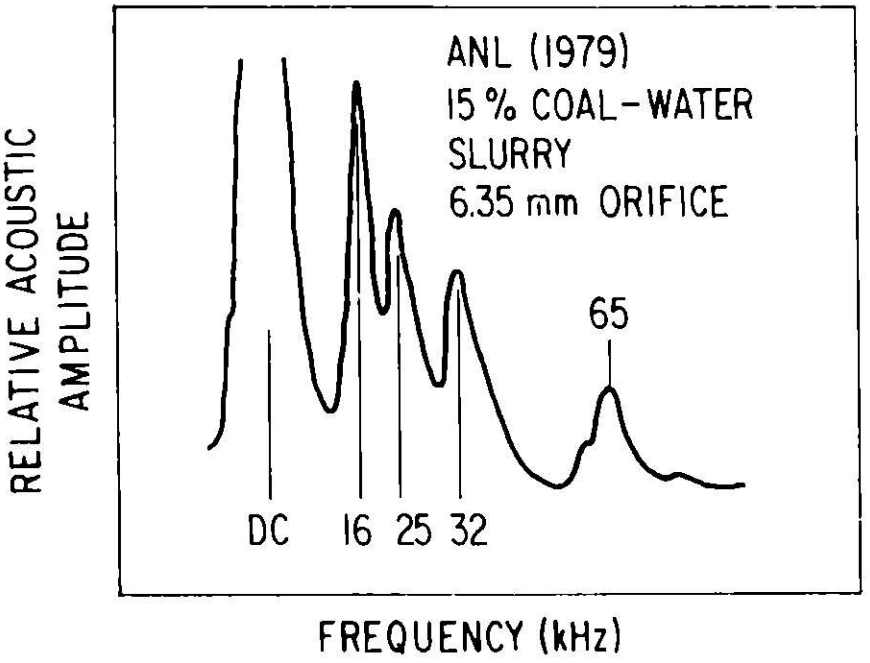

Fig. 7. A Typical Acoustic Spectrum Obtained from a 20% Coal Slurry Flowing through a 6.35-mm Orifice. Peaks of interest from right to left are 65, 32, 25 and 16 kHz. ANL Neg. No. 306-79-893.

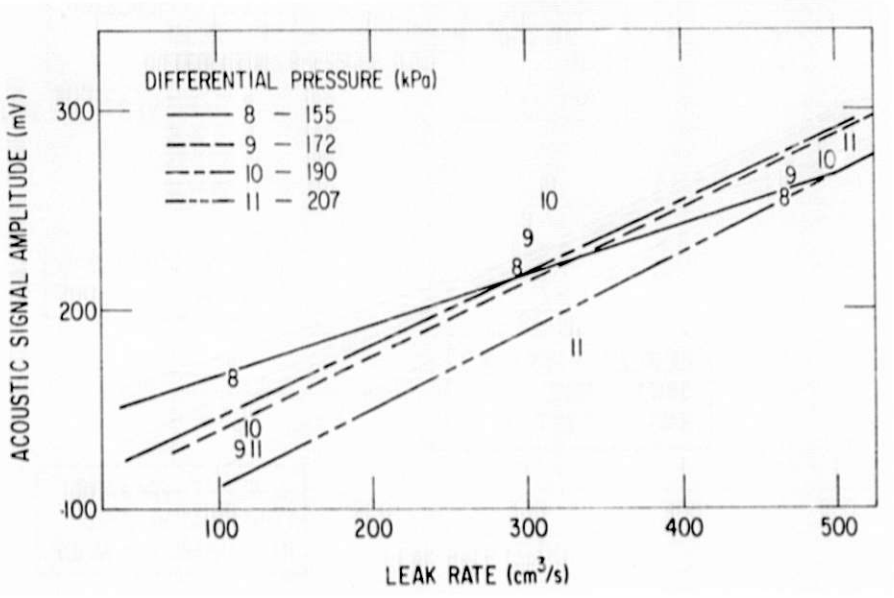

Fig. 8. Acoustic Signal Amplitude vs Leakage Rate for Higher Differential Pressure Ranges. Note that the data show a wide scatter and that for a given signal level the leakage rate can vary by 100 cm^3/s. However, note that the acoustic signal level increases by a factor of 2 between no flow and 500 cm^3/s. ANL Neg. No. 306-79-892.

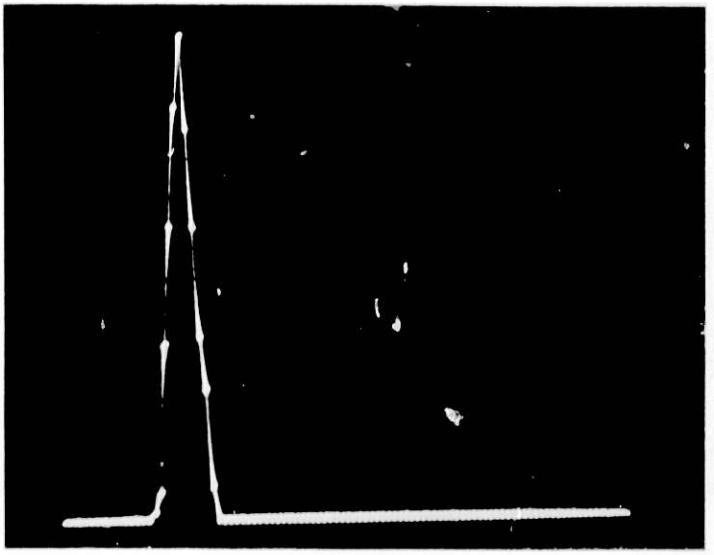

(a)

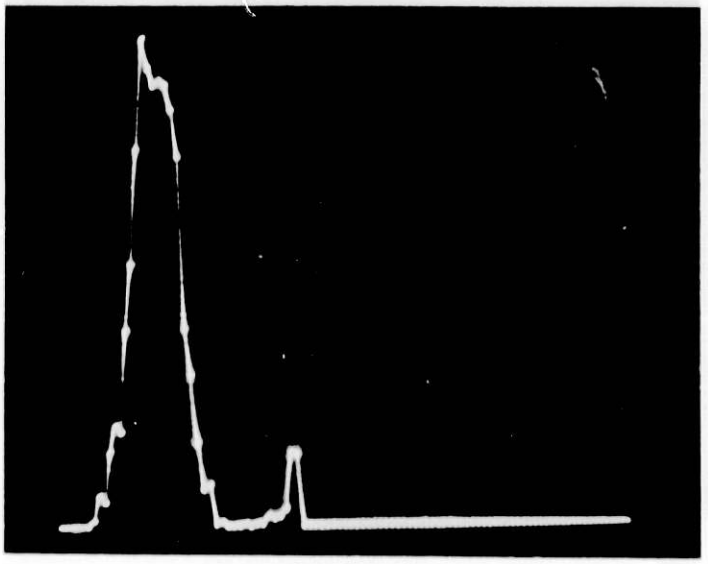

(b)

Fig. 9. Probability Distribution Function of Flow-induced Signal Amplitude. (a) Distribution function of acoustic signal amplitude taken at 172 kPa differential pressure. This is typical of the distribution of acoustic amplitudes in the higher and more stable range. Horizontal scale is rms amplitude. Vertical scale is probability. ANL Neg. No. 306-79-802. (b) Distribution function of acoustic signal taken at 121 kPa. The wide and nonsymmetric distribution is due to the unstable differential pressure. ANL Neg. No. 306-79-801.

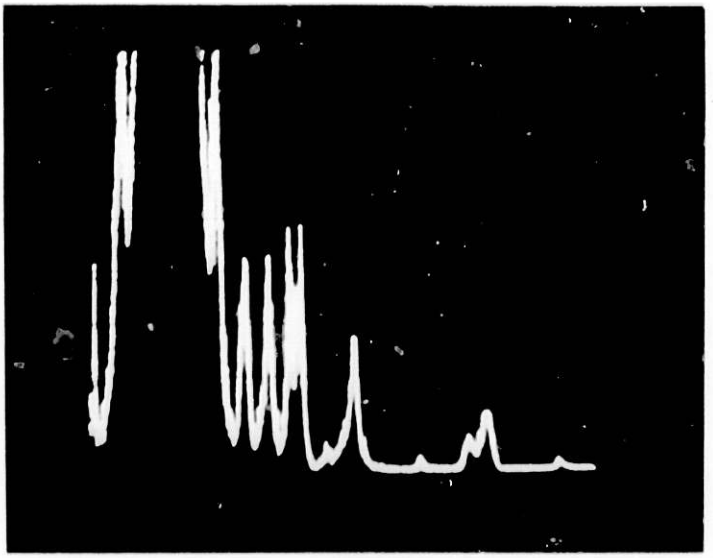

(a)

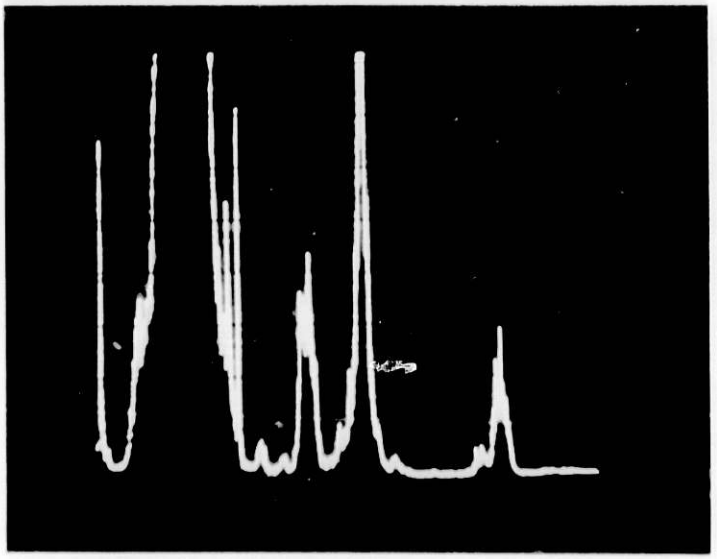

(b)

Fig. 10. Spectral Distribution of Acoustic Signal Taken from Converging Orifices. (a) 6.35- to 3.18-mm-diameter orifice. ANL Neg. No. 306-79-804. (b) 9.52- to 6.35-mm-diameter orifice. ANL Neg. No. 306-79-803. Both were obtained at 138 kPa differential pressure using a 45-kHz center-frequency filter with a 1-kHz bandwidth. Horizontal scale is 10 kHz/division. Both spectra show peaks at 25, 35, and 63 kHz.

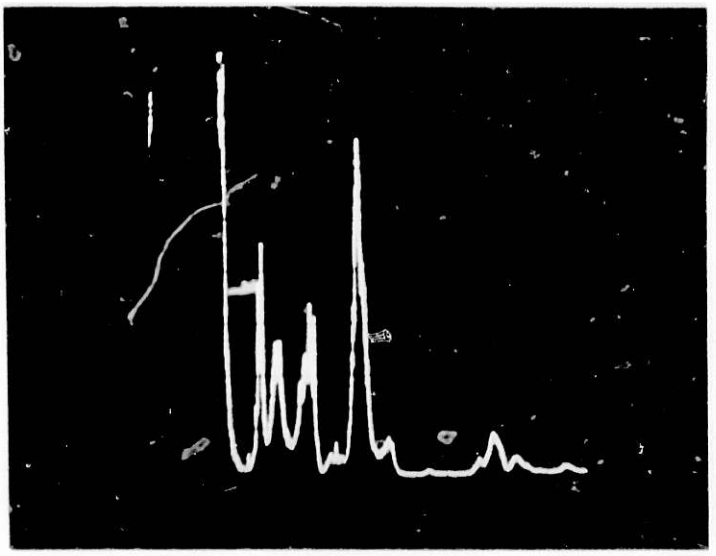

(a)

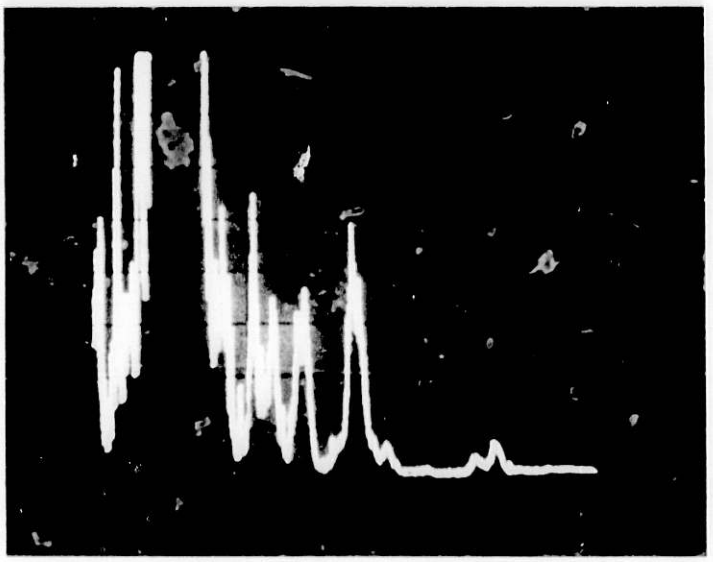

(b)

Fig. 11. Spectral Distribution of Acoustic Signal Taken from Diverging Orifices. (a) 3.18- to 6.35-mm-diameter orifice. ANL Neg. No. 306-79-806. (b) 6.35- to 9.52-mm-diameter orifice. ANL Neg. No. 306-79-805. Both were obtained at 138 kPa differential pressure using a 35-kHz center-frequency filter with a 1-kHz bandwidth. Horizontal scale is 10 kHz/division. Both spectra show peaks at 25, 35, and 63 kHz.

Task D -- Corrosion Behavior of Materials in Coal-conversion Processes

1. Corrosion in Gasification Environments *(K. Natesan)*

The objectives of this program are to (1) develop uniaxial tensile data on four commercial alloys exposed to multicomponent gas environments, (2) experimentally evaluate the high-temperature corrosion behavior of iron- and nickel-base alloys in gas environments with a wide range of oxygen, sulfur, and carbon potentials, and (3) develop a systems approach, based upon available thermodynamic and kinetic information, to evaluate possible corrosion problems in different coal-conversion processes.

The experimental program to generate uniaxial tensile data on four iron- and nickel-base alloys exposed to multicomponent gas environments was discussed previously.[11] The experimental apparatus and the chemical composition of the alloys and gas mixtures used in this program were described in detail.[12] Calculated values for the oxygen and sulfur partial pressures established by the gas mixtures in different runs have also been reported.[13]

During the present quarter, 1000-h exposures of corrosion and uniaxial tensile specimens to gas mixtures 1B and 2B at 982°C were completed. In another experimental run, specimens were exposed at 750°C to mixture 1A in the absence of steam to simulate the environment that was used in the experiment at Battelle Columbus Laboratory. Similar exposures are continuing at temperatures of 871 and 982°C. Postexposure tensile tests of the specimens are being conducted in vacuum at an initial strain rate of $4.1 \times 10^{-4} s^{-1}$. The corrosion specimens from different experiments are being examined by scanning-electron microscopy with an energy-dispersive x-ray analyzer or an electron microprobe.

Tensile data obtained thus far from specimens exposed to different mixed-gas environments were analyzed to determine the changes in the tensile properties due to variations in oxygen and sulfur partial pressures in the gas environment. Figures 12-15 show the engineering stress-engineering strain curves for Incoloy 800, Type 310 stainless steel, Inconel 671, and U.S. Steel Alloy 18-18-2, respectively, in the as-received and thermally aged conditions, and after 1000-h exposure to gas mixtures with different oxygen, sulfur, and carbon potentials at 982°C. Similar curves for the alloys exposed at 871°C (except U. S. Steel Alloy 18-18-2) are shown in Figs. 16-18. Thermal aging has little effect on the tensile properties of these alloys, with the exception of Inconel 671, which is a two-phase nickel-base alloy containing 48 wt % Cr and 0.35 wt % Ti. In general, the results for all four alloys show that the ultimate tensile strength decreases after exposure to complex gas mixtures when compared with those of the material in the as-received and thermally aged conditions.

a. Effect of Alloying Additions on the Corrosion Behavior of Type 310 Stainless Steel

It has been fairly well established that sulfidation is the major mode of material degradation in environments that are prevalent in coal-gasification systems.[14] Therefore, it is essential that the alloys used develop a protective oxide scale during the service life of the component.

The results from various experimental programs have clearly shown that in all the Fe-, Ni-, and Co-base alloys, a high chromium concentration is essential for the formation of a continuous oxide scale on surfaces exposed to complex gas environments. Since the mode of interaction between these materials and mixed-gas environments is the formation of Cr-rich oxide or sulfides, it is pertinent to consider the thermodynamic stability of the oxides and sulfides of different alloying elements relative to those of chromium. Elements that form oxides and sulfides of greater stability than those of chromium are indicated in Fig. 19. The alloying elements Mn and Si, which form oxides more stable than chromium oxide, have a tendency to migrate from the bulk of the alloy to the scale/substrate interface and/or to the scale itself. However, at higher concentrations of Mn, the formation of manganese sulfide is a distinct possibility and can lead to enhanced corrosion rates as observed by Perkins and Bhat.[15] In the oxide mode of interaction, Mn preferentially segregates in the scale and has been found to have an adverse effect on the scale spallation, leading to enhanced corrosion rates.[16-18] The breakaway corrosion behavior observed[19] in Type 310 stainless steel after a 2000-h exposure to a Metal Properties Council (MPC)-selected gas mixture may be due to migration of Mn to the scale region and scale spallation. In oxidation studies on Fe-Cr-Ni alloys, a silicon content of up to 4 wt % has been found to promote the formation of protective layers; however, a silicon concentration as low as 2 wt % seems to alter the mode of attack from oxidation to sulfidation upon exposure of the steel to complex gas environments, as shown for U. S. Steel Alloy Fe-18 wt % Cr-18 wt % Ni-2 wt % Si.[20]

The effect of titanium on the corrosion behavior of Type 310 stainless steel in mixed-gas environments has been studied by additions of up to 3 wt % of the element. During the present quarter, thermogravimetric studies were conducted to evaluate the effects of titanium additions on behavior in multicomponent gas environments with various oxygen and sulfur partial pressures. The compositions of the commercial and titanium-modified Type 310 stainless steel are given in Table IV. Figures 20-23 show the weight gain as a function of time for the two materials in environments with different oxygen and sulfur partial pressures. The test conditions and the types of scale developed on the specimens are listed in Table V. The preliminary results show that at $p_{O_2} = 5.7 \times 10^{-17}$ atm and $p_{S_2} = 9.9 \times 10^{-6}$ atm, both alloys developed Cr-rich sulfide scales and showed significant weight gain. At lower sulfur partial pressures, Type 310 stainless steel developed a Cr-rich oxide scale while the titanium-modified steel showed a (Cr,Ti) oxide scale. In all the experiments of the present investigation, the modified steel exhibited higher corrosion rates than the commercial steel. The specimens are being examined to evaluate the intergranular penetration of sulfur. Additional experiments are being conducted to quantify the titanium effects on the corrosion behavior of the steel as a function of the exposure environment.

TABLE IV. Composition of Steels Used in the Program

Alloy	Element, wt %					
	Cr	Ni	Mn	Si	Ti	Fe
Type 310 SS	24.2	19.5	1.5	0.4	-	Balance
Ti-modified Type 310 SS[a]	25.0	20.0	-	-	2.9	Balance

[a]Supplied by Sandia Laboratories, Livermore, CA.

TABLE V. Experimental Conditions and Types of Scale Observed on the Specimens After Exposure at 1000°C

p_{O_2}, atm	p_{S_2}, atm	a_c	Type of Scale	
			Type 310 SS	Ti-modified Type 310 SS
5.7×10^{-17}	9.9×10^{-6}	0.024	Cr-rich Sulfide	Cr-rich Sulfide
3.4×10^{-16}	1.3×10^{-6}	0.017	Cr-rich Oxide	(Cr,Ti) Oxide
1.9×10^{-16}	5.2×10^{-7}	0.020	Cr-rich Oxide	(Cr,Ti) Oxide
1.2×10^{-16}	1.6×10^{-7}	0.022	Cr-rich Oxide	(Cr,Ti) Oxide

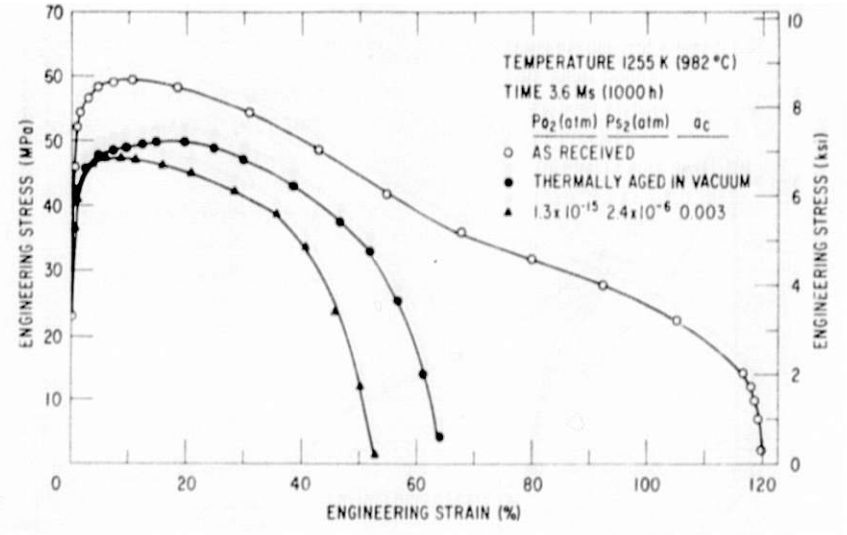

Fig. 12. Engineering Stress-Engineering Strain Behavior for Incoloy 800 in the As-received and Thermally Aged Conditions and After 1000-h Exposures to Complex Gas Mixtures at 982°C. ANL Neg. No. 306-79-86.

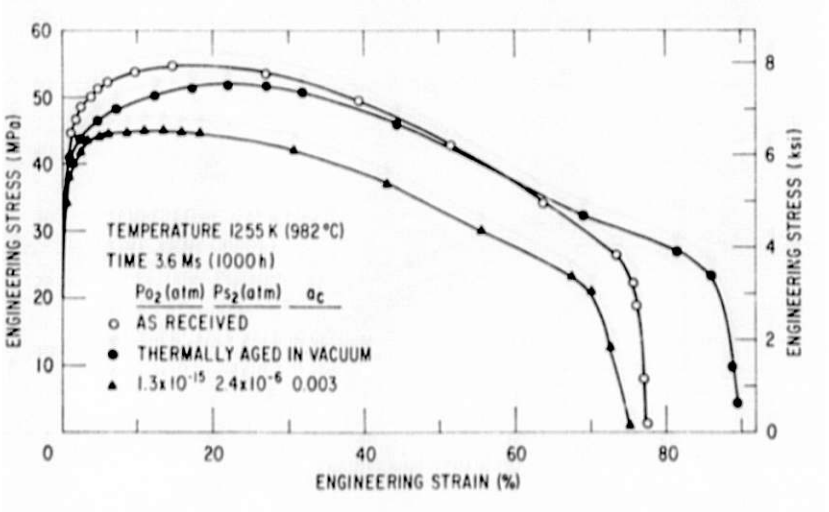

Fig. 13. Engineering Stress-Engineering Strain Behavior for Type 310 Stainless Steel in the As-received and Thermally Aged Conditions and After 1000-h Exposures to Complex Gas Mixtures at 982°C. ANL Neg. No. 306-79-95.

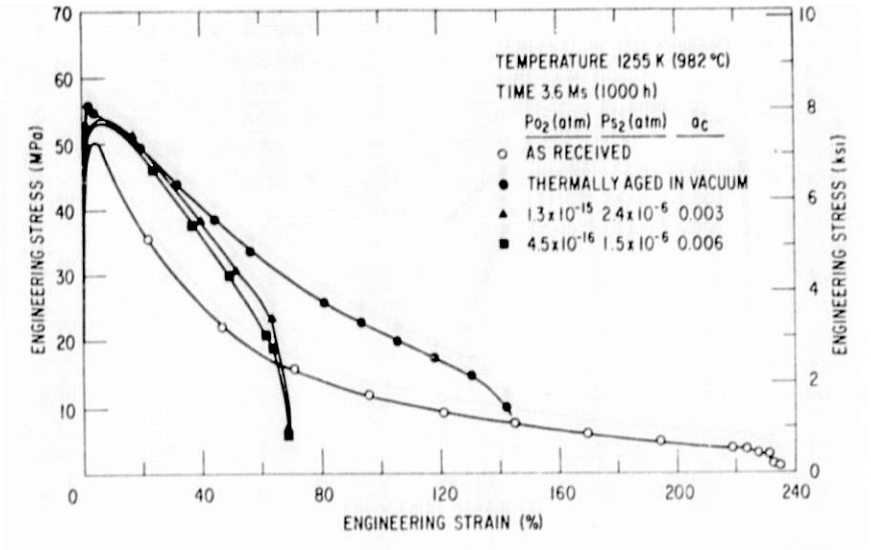

Fig. 14. Engineering Stress-Engineering Strain Behavior for Inconel 671 in the As-received and Thermally Aged Conditions and After 1000-h Exposures to Complex Gas Mixtures at 982°C. ANL Neg. No. 306-79-76.

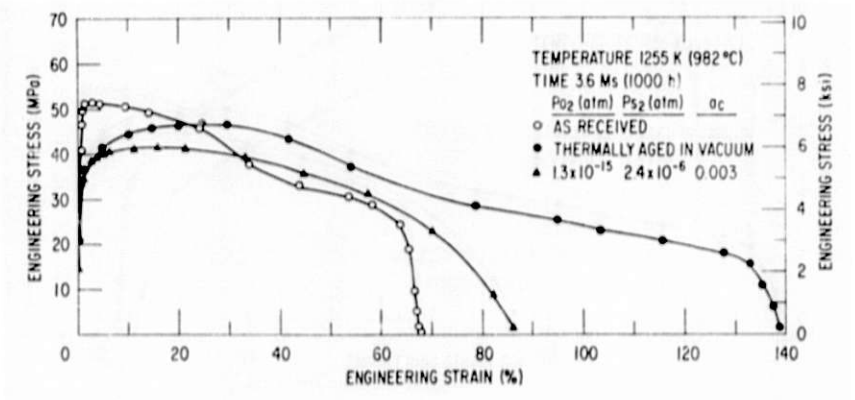

Fig. 15. Engineering Stress-Engineering Strain Behavior for U.S. Steel Alloy 18-18-2 in the As-received and Thermally Aged Conditions and After 1000-h Exposures to Complex Gas Mixtures at 982°C. ANL Neg. No. 306-79-80.

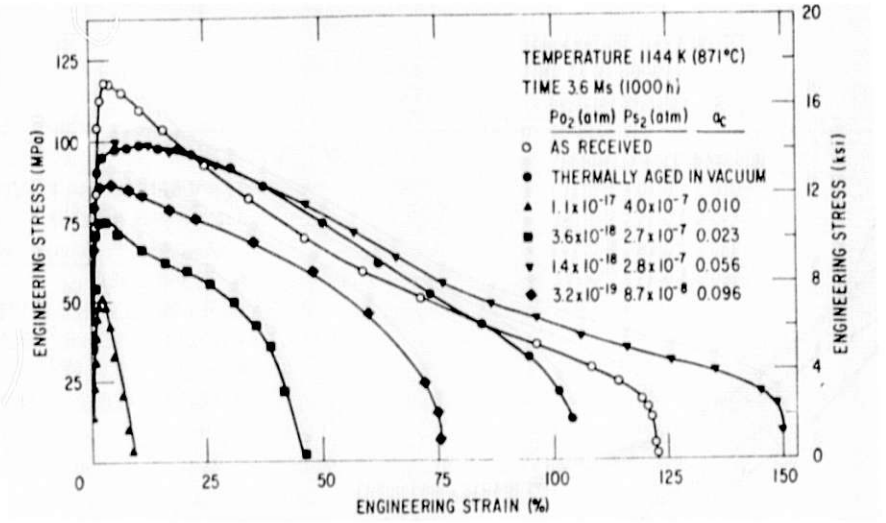

Fig. 16. Engineering Stress-Engineering Strain Behavior for Incoloy 800 in the As-received and Thermally Aged Conditions and After 1000-h Exposures to Complex Gas Mixtures at 871°C. ANL Neg. No. 306-79-93.

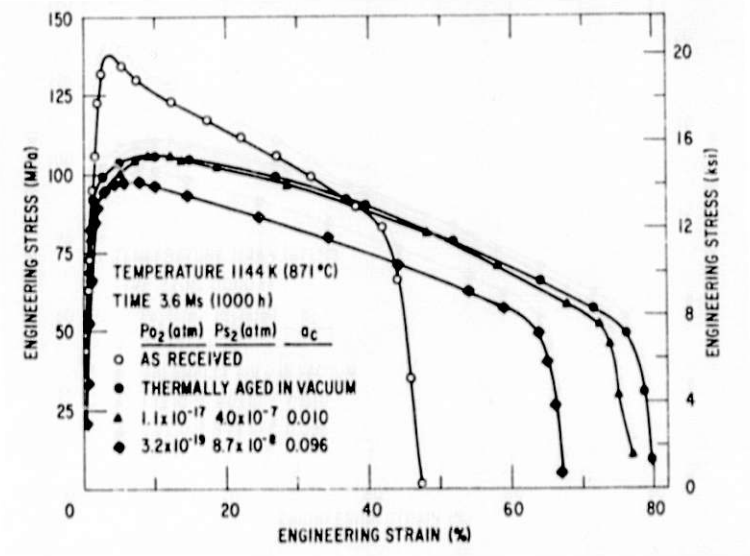

Fig. 17. Engineering Stress-Engineering Strain Behavior for Type 310 Stainless Steel in the As-received and Thermally Aged Conditions and After 1000-h Exposures to Complex Gas Mixtures at 871°C. ANL Neg. No. 306-79-91.

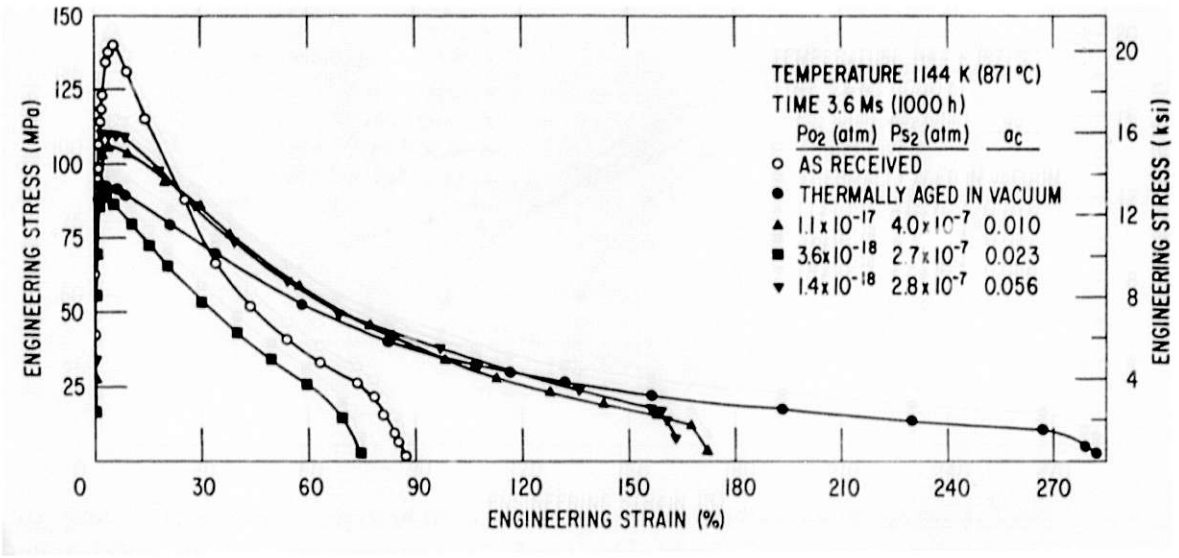

Fig. 18. Engineering Stress-Engineering Strain Behavior for Inconel 671 in the As-received and Thermally Aged Conditions and After 1000-h Exposures to Complex Gas Mixtures at 871°C. ANL Neg. No. 306-79-84.

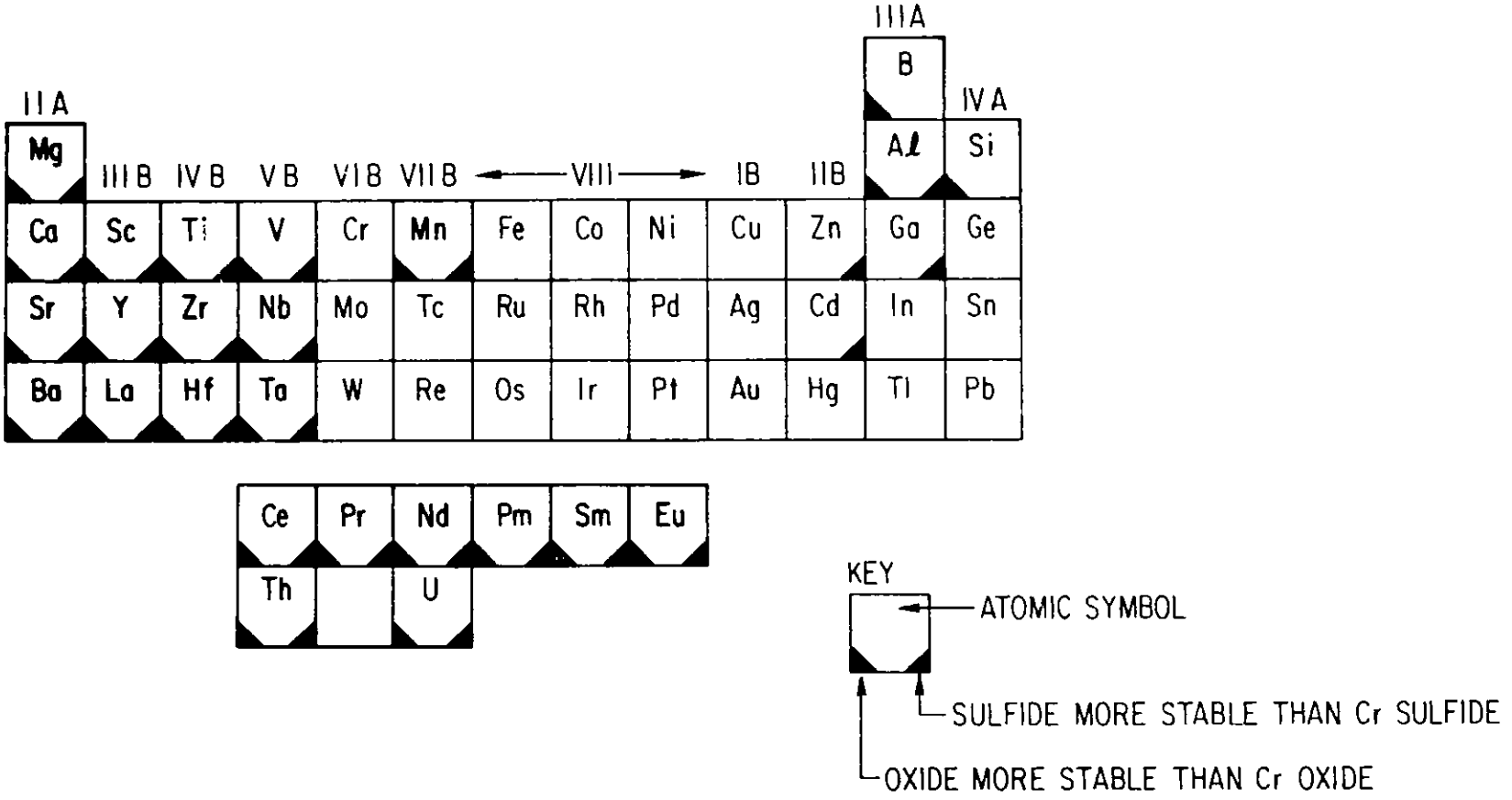

Fig. 19. Periodic Table Showing Elements Which Form Oxides and Sulfides of Greater Stability Than Chromium Oxide and Chromium Sulfide. ANL Neg. No. 306-79-105R.

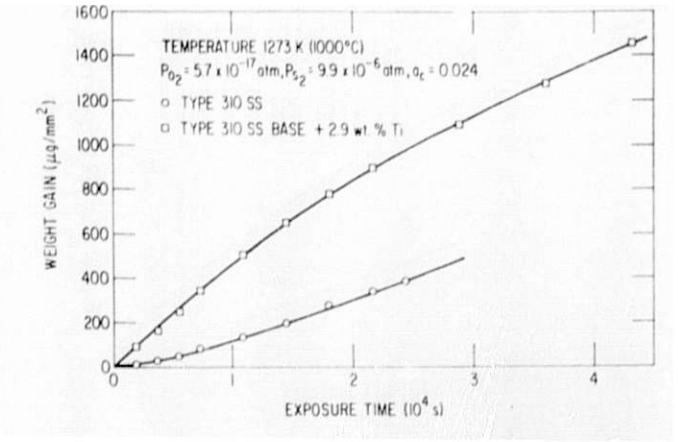

Fig. 20. Weight Gain vs Time Curves for Commercial and Ti-modified Type 310 Stainless Steel After Exposure at 1000°C to a Mixed Gas Environment with p_{O_2} = 5.7 x 10^{-17} atm, p_{S_2} = 9.9 x 10^{-6} atm, and a_c = 0.024. ANL Neg. No. 306-79-869.

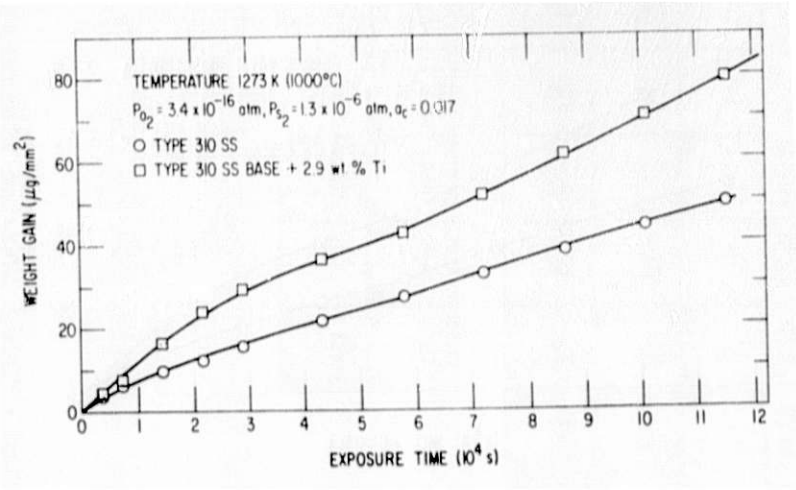

Fig. 21. Weight Gain vs Time Curves for Commercial and Ti-modified Type 310 Stainless Steel After Exposure at 1000°C to a Mixed Gas Environment with p_{O_2} = 3.4 x 10^{-16} atm, p_{S_2} = 1.3 x 10^{-6} atm, and a_c = 0.017. ANL Neg. No. 306-79-866.

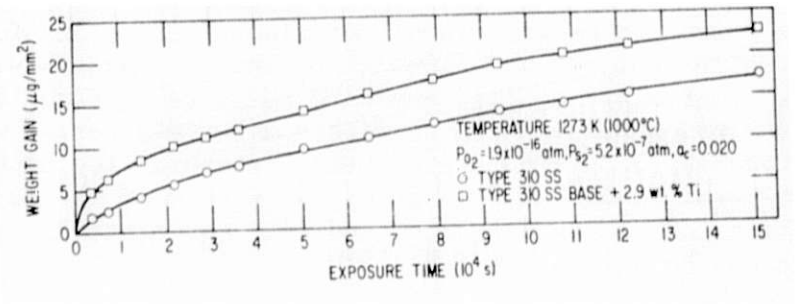

Fig. 22. Weight Gain vs Time Curves for Commercial and Ti-modified Type 310 Stainless Steel After Exposure at 1000°C to a Mixed Gas Environment with p_{O_2} = 1.9 x 10^{-16} atm, p_{S_2} = 5.2 x 10^{-7} atm, and a_c = 0.020. ANL Neg. No. 306-79-862.

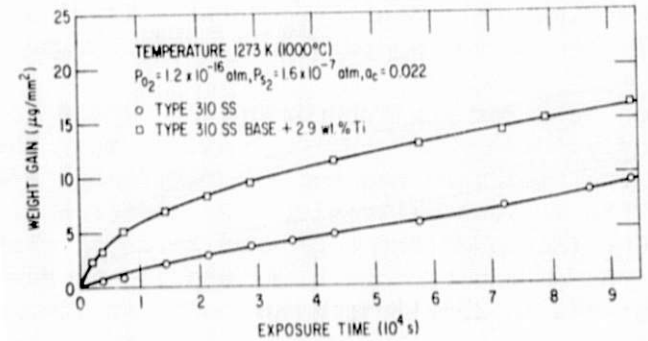

Fig. 23. Weight Gain vs Time Curves for Commercial and Ti-modified Type 310 Stainless Steel After Exposure at 1000°C to a Mixed Gas Environment with p_{O_2} = 1.2 x 10^{-16} atm, p_{S_2} = 1.6 x 10^{-7} atm, and a_c = 0.022. ANL Neg. No. 306-79-864.

2. Effect of Sulfation Accelerators and Corrosion Inhibitors on Materials in Fluidized-bed Combustion Systems *(O.K. Chopra)*

a. Introduction

The sulfation rate and the extent of sulfation of many limestones can be enhanced by impregnating the stone with sulfation accelerators, such as NaCl, $CaCl_2$, or Na_2CO_3. However, the use of salts in fluidized-bed combustion systems requires an evaluation of the possible effects of these constituents on the corrosion of structural materials to identify factors that could decrease the reliability and lifetime of system components. The objectives of this program are to (a) evaluate the effect of sulfation accelerators on the corrosion behavior of candidate materials for an atmospheric-pressure fluidized-bed combustion system, (b) determine the types of deposits formed on metal surfaces, (c) study the nature of the corrosion reactions resulting from these deposits, and (d) correlate the corrosion results with process conditions.

The process development unit atmospheric-pressure fluidized-bed coal-combustion (AFBC) facility at Argonne National Laboratory was used to conduct the corrosion tests. Four 100-h corrosion tests with and without sulfation accelerators have been completed in the AFBC facility. In each test, three air-cooled corrosion probes and four corrosion coupon holders, each holding seven specimens, were installed at various locations in the fluidized bed and the freeboard sections of the combustor. The experimental conditions for the corrosion tests are given in Table VI. The materials, specimen locations, and temperature of the corrosion probes for the four corrosion experiments were given earlier.[10,21]

The corrosion specimens were examined metallographically to evaluate the corrosion behavior in terms of an average thickness of the surface scale and average depth of internal corrosive penetration in the specimens. Measurements were made at several locations on the specimens to obtain an average value. The distribution and nature of the corrosion products was evaluated by energy dispersive x-ray and electron microprobe analyses.

The corrosion behavior for the corrosion coupons from all the tests were described previously.[10,21] The results indicate that the addition of 0.3 mol % $CaCl_2$ to the fluidized bed had no significant effect on the corrosion behavior of the various materials. The addition of 0.5 mol % NaCl or 1.9 mol % Na_2CO_3 increased the corrosion rates of most of the materials. In general, the austenitic stainless steels and Haynes Alloy 188 exhibited better resistance to accelerated corrosion in the presence of salts than the high-nickel alloys. The various materials that were located in the freeboard section of the combustor at temperatures between 800 and 975 K showed no detectable corrosion, with the exception of Fe-9Cr-1Mo steel (alloy C-12), which was oxidized.

During the present reporting period, metallographic examination of the air-cooled tubular specimens, which were located inside the fluidized bed, has been completed; the corrosion results are presented below.

b. Results

The air-cooled tubular specimens located inside the fluidized bed had thin surface scales and 20- to 80-μm-thick deposits from the bed material. The corrosion behavior of the specimens was not uniform, owing to variations in the nature of the deposit on the specimen surface. For example, corrosion was greater under deposits which contained significant amount of ash than in regions where the deposits consisted mainly of the limestone material. In a fluidized-bed environment, the nature of the deposits on the surface of the tubes can vary depending on the position of the surface with respect to the flow of the fluidizing gas and bed material. Consequently, the orientation of the specimen surface inside the combustor was marked on each specimen and the thickness of the surface scale and depth of corrosive penetration was measured at intervals of ∿ 20° around the circumference of the specimens. The average values for the temperature and corrosion of the specimens exposed inside the fluidized bed in the four corrosion tests are given in Tables VII-X. For the air-cooled corrosion probes, the temperature of three of the seven specimens was monitored during the test. The average temperature of the remaining corrosion specimens was obtained from the temperature profile along the length of the probe. The average temperature of the various corrosion specimens varied from 800 to 1000 K.

The results show that at temperatures between 800 and 1000 K, the addition of salt, i.e., NaCl, $CaCl_2$, or Na_2CO_3, had no effect on the corrosion behavior of any of the materials. In general, corrosion specimens of the various iron-and nickel-base alloys containing > 15% chromium had 2- to 3-μm-thick surface scale with internal corrosive attack to a depth of 2-5 μm. The total corrosion in the specimens from test CT-1, without the addition of salt, was somewhat greater than that for the other corrosion tests because the average temperature of the specimens during this test was ∿ 50 K higher. Micrographs of the cross section of Type 310 stainless steel, Incoloy 800, Inconel 601, and RA 333 specimens from the four corrosion tests are shown in Figs. 24 and 25.

Micrographs of Fe-2-1/4Cr-1Mo and Fe-9Cr-1Mo steel specimens from the four corrosion tests are shown in Figs. 26 and 27, respectively. In these specimens the thickness of the surface scale and the depth of internal corrosion was relatively small compared to the thickness of the scale. For the various experimental conditions in the four runs, the average values of the total corrosion for Fe-2-1/4Cr-1Mo and Fe-9Cr-1Mo specimens were ∿ 135 and ∿ 15 μm, respectively, at temperatures near 900°C. The corrosion scales on these steels were quite porous and indicated an interaction with the deposits from the bed material. Similar behavior was observed in several high-chromium alloys, e.g., Type 309 stainless steel and Incoloy 800.

The distribution and nature of the corrosion products in the surface scales was investigated by electron microprobe analyses. The x-ray images for Fe, O, Cr, Ca, S, Si, and K in the scales observed on Fe-2-1/4Cr-1Mo and Fe-9Cr-1Mo specimens are shown in Figs. 28 and 29, respectively. The results indicate that the scales consist of two distinct layers; an inner layer of a mixed oxide of iron and chromium and an outer layer containing various elements (e.g., Fe, O, Ca, S, Si, and K) from the bed material. The presence of these elements indicates that the outer layer of the scale forms

by the interaction of the deposits with the scale whereas the inner layer forms by corrosion of the material. For the Fe-9Cr-1Mo steel the extent of interaction between the deposits and the scale is less than that for Fe-2-1/4Cr-1Mo steel. This difference is probably due to the higher concentration of chromium in the surface scale of Fe-9Cr-1Mo steel.

The corrosion behavior of the air-cooled specimens, which were exposed in the freeboard region of the combustor, is being evaluated. The results will provide a better understanding of the mechanisms of the reaction between the deposits and the scale. Longer-duration (500 to 1000 h) corrosion tests are being conducted to further evaluate the effect of salts on the performance of various structural materials in the fluidized-bed combustion environment.

TABLE VI. Calcium-to-Sulfur Molar Ratios Required to Maintain 700 ppm SO_2 in the Dry Off-Gas

Run No.	Treatment	Ca/S Molar Ratio
CT-1	None	3.4
CT-2	0.3 mol % $CaCl_2$	3.5
CT-3	0.5 mol % NaCl	3.6
CT-4	1.9 mol % Na_2CO_3	2.0

Experimental Conditions:

Bed Temperature - 850°C
Pressure - 101.3 kPa (1 atm)
Fluidizing Velocity - 1 m/s
Fluidized-bed Height - 813 mm
Excess O_2 - 3% in dry off-gas
Coal - Sewickley (-12 +100 mesh), 5.46% S
Sorbent - Grove limestone (-10 +30 mesh), 95.3% $CaCO_3$

TABLE VII. Average Values of the Thickness of Surface Scale and Internal Corrosive Penetration Measured in Air-cooled Corrosion Specimens for Run CT-1

Specimen Holder[a]	Material	Average Temperature, K	Surface-scale thickness, μm	Corrosive Penetration, μm	Total Corrosive Attack, μm	Remarks
AC-2	Inconel 601	876	2.6	4.7	7.3	Maximum corrosive attack ∿ 15 μm
AC-2	Inconel 617	970	2.5	2.6	5.1	
AC-2	RA 333	985	2.4	4.5	6.9	
AC-1	Type 304 SS	1000	2.3	2.7	5.0	
AC-1	Type 309 SS	1000	5.6	5.9	11.5	Interaction between surface scale and deposits
AC-2	Type 310 SS	925	4.9	6.9	11.8	Interaction between surface scale and deposits
AC-1	Type 316 SS	985	2.4	4.1	6.5	
AC-2	Type 321 SS	900	2.9	2.1	5.0	
AC-1	Incoloy 800	950	3.2	3.6	6.8	Interaction between surface scale and deposits
AC-2	Incoloy 800	950	2.5	3.9	6.4	Interaction between surface scale and deposits
AC-1	Type 446 SS	876	2.1	2.2	4.3	
AC-1	9Cr-1Mo Steel	970	-	-	18.4	Maximum corrosion ∿ 35 μm
AC-1	2-1/4Cr-1Mo Steel	925	-	-	171.9	Maximum corrosion ∿ 320 μm

[a]The air-cooled corrosion probes AC-1 and AC-2 were located inside the fluidized bed at distances of 508 and 305 mm, respectively, above the fluidizing gas distributor plate.

TABLE VIII. Average Values of the Thickness of Surface Scale and Internal Corrosive Penetration Measured in Air-cooled Corrosion Specimens for Run CT-2

Specimen Holder[a]	Material	Average Temperature, K	Surface-scale thickness, μm	Corrosive Penetration, μm	Total Corrosive Attack, μm	Remarks
AC-2	Inconel 601	840	1.7	1.8	3.5	
AC-2	Inconel 601	936	2.2	2.6	4.8	
AC-2	RA 333	950	3.0	6.2	9.2	Internal corrosion mainly sulfides
AC-1	Type 304 SS	800	1.2	1.6	2.8	
AC-1	Type 309 SS	870	2.0	3.5	5.5	
AC-2	Type 309 SS	958	2.0	4.1	6.1	
AC-2	Type 310 SS	896	2.3	5.0	7.3	
AC-1	Type 316 SS	856	1.2	2.1	3.3	
AC-2	Type 321 SS	870	2.1	2.0	4.1	
AC-1	Incoloy 800	833	2.3	3.5	5.8	
AC-2	Incoloy 800	919	1.7	3.7	5.4	
AC-1	Type 446 SS	780	2.1	2.8	4.9	
AC-1	9Cr-1Mo Steel	848	-	-	12.9	Maximum corrosion ∿ 25 μm
AC-1	2-1/4Cr-1Mo Steel	817	-	-	142.3	Maximum corrosion ∿ 160 μm

[a]The air-cooled corrosion probes AC-1 and AC-2 were located inside the fluidized bed at distances of 508 and 305 mm, respectively, above the fluidizing gas distributor plate.

TABLE IX. Average Values of the Thickness of Surface Scale and Internal Corrosive Penetration Measured in Air-cooled Corrosion Specimens for Run CT-3

Specimen Holder[a]	Material	Average Temperature, K	Surface-scale Thickness, μm	Corrosive Penetration, μm	Total Corrosive Attack, μm	Remarks
AC-2	Inconel 601	802	1.9	1.7	3.6	Corrosion in some regions ∿ 10 μm
AC-2	Inconel 617	873	2.7	3.8	6.5	
AC-2	RA 333	878	2.0	1.7	3.7	Corrosion in some regions ∿ 10 μm
AC-1	Type 304 SS	861	2.4	1.7	4.1	
AC-2	Type 304 SS	862	1.6	1.2	2.8	
AC-2	Type 309 SS	878	1.7	1.9	3.6	
AC-2	Type 310 SS	843	2.5	1.0	3.5	
AC-1	Type 316 SS	903	1.8	2.3	4.1	
AC-1	Type 321 SS	907	2.2	3.5	5.7	
AC-2	Type 321 SS	823	3.1	3.2	6.3	Intergranular attack
AC-1	Incoloy 800	885	2.4	4.0	6.4	
AC-1	Type 446 SS	850	3.0	3.2	6.2	Intergranular attack
AC-1	9Cr-1Mo Steel	895	-	-	16.5	Maximum corrosion ∿ 40 μm
AC-1	2-1/4Cr-1Mo Steel	873	-	-	101.0	Maximum corrosion ∿ 140 μm

[a]The air-cooled corrosion probes AC-1 and AC-2 were located inside the fluidized bed at distances of 305 and 508 mm, respectively, above the fluidizing gas distributor plate.

TABLE X. Average Values of the Thickness of Surface Scale and Internal Corrosive Penetration Measured in Air-cooled Corrosion Specimens for Run CT-4

Specimen Holder[a]	Material	Average Temperature, K	Surface-scale Thickness, μm	Corrosive Penetration, μm	Total Corrosive Attack, μm	Remarks
AC-2	Inconel 601	890	2.1	1.4	3.5	
AC-2	Inconel 617	933	1.3	1.4	2.7	
AC-2	RA 333	940	2.1	3.2	5.3	
AC-1	Type 304 SS	823	2.2	1.7	3.9	
AC-1	Type 309 SS	878	2.7	3.8	6.5	
AC-2	Type 309 SS	948	4.2	5.3	9.5	Interaction between surface scale and deposits
AC-2	Type 310 SS	913	2.1	2.1	4.7	
AC-1	Type 316 SS	878	2.2	2.1	4.3	
AC-2	Type 321 SS	901	2.3	1.9	4.2	
AC-1	Incoloy 800	862	2.6	3.0	5.6	
AC-2	Incoloy 800	923	2.5	3.1	5.6	Interaction between surface scale and deposits
AC-1	Type 446 SS	802	2.4	1.0	3.4	
AC-1	9Cr-1Mo Steel	873	-	-	13.2	Maximum corrosion ∿ 25 μm
AC-1	2-1/4Cr-1Mo Steel	843	-	-	119.5	Maximum corrosion ∿ 180 μm

[a]The air-cooled corrosion probes AC-1 and AC-2 were located inside the fluidized bed at distances of 508 and 305 mm, respectively, above the fluidizing gas distributor plate.

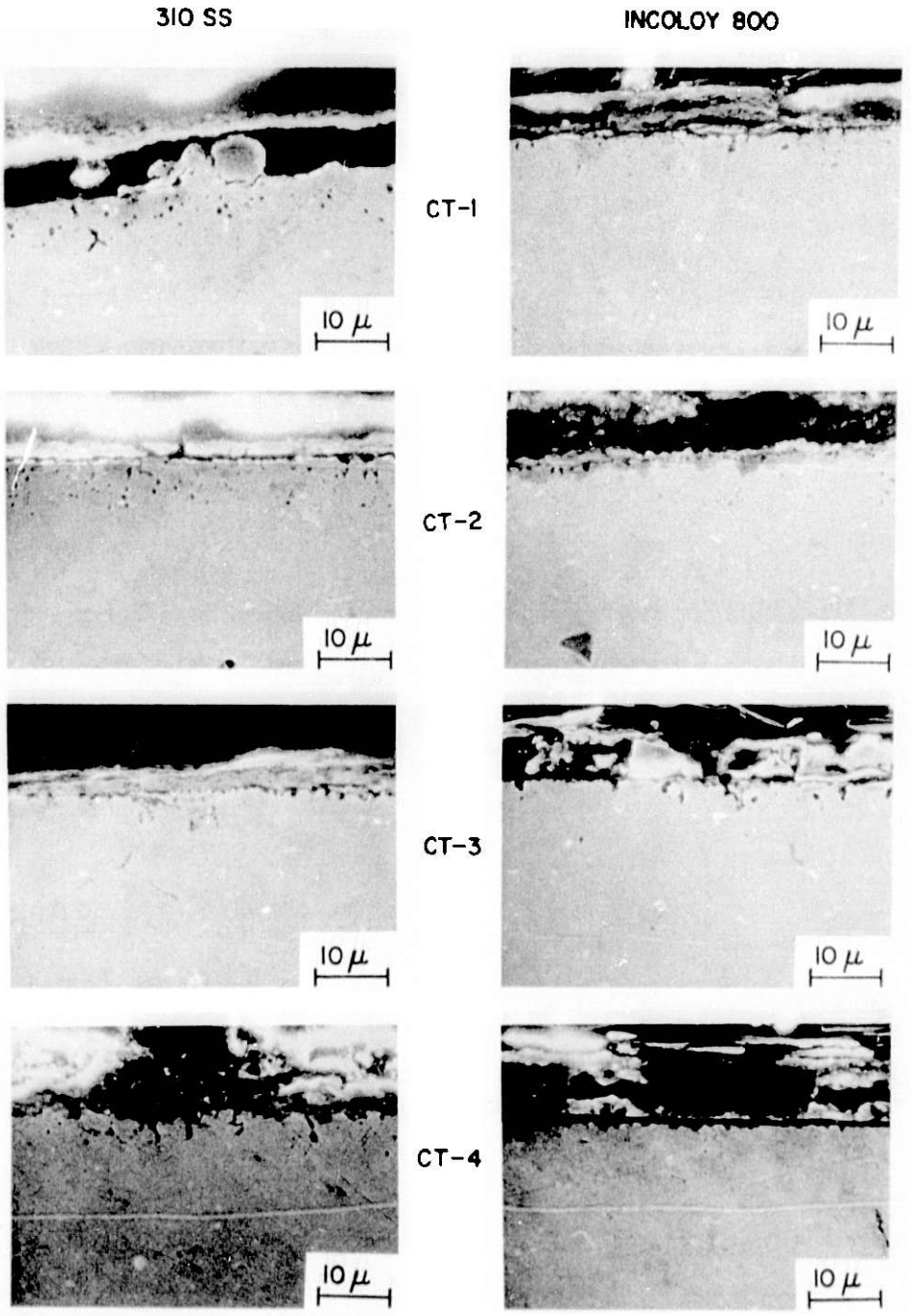

Fig. 24. SEM Micrographs of Type 310 Stainless Steel and Incoloy 800 After a 100-h Exposure Inside the Fluidized Bed. CT-1, without salt; CT-2, 0.3 mol % $CaCl_2$; CT-3, 0.5 mol % NaCl; and CT-4, 1.9 mol % Na_2CO_3. ANL Neg. No. 306-79-681.

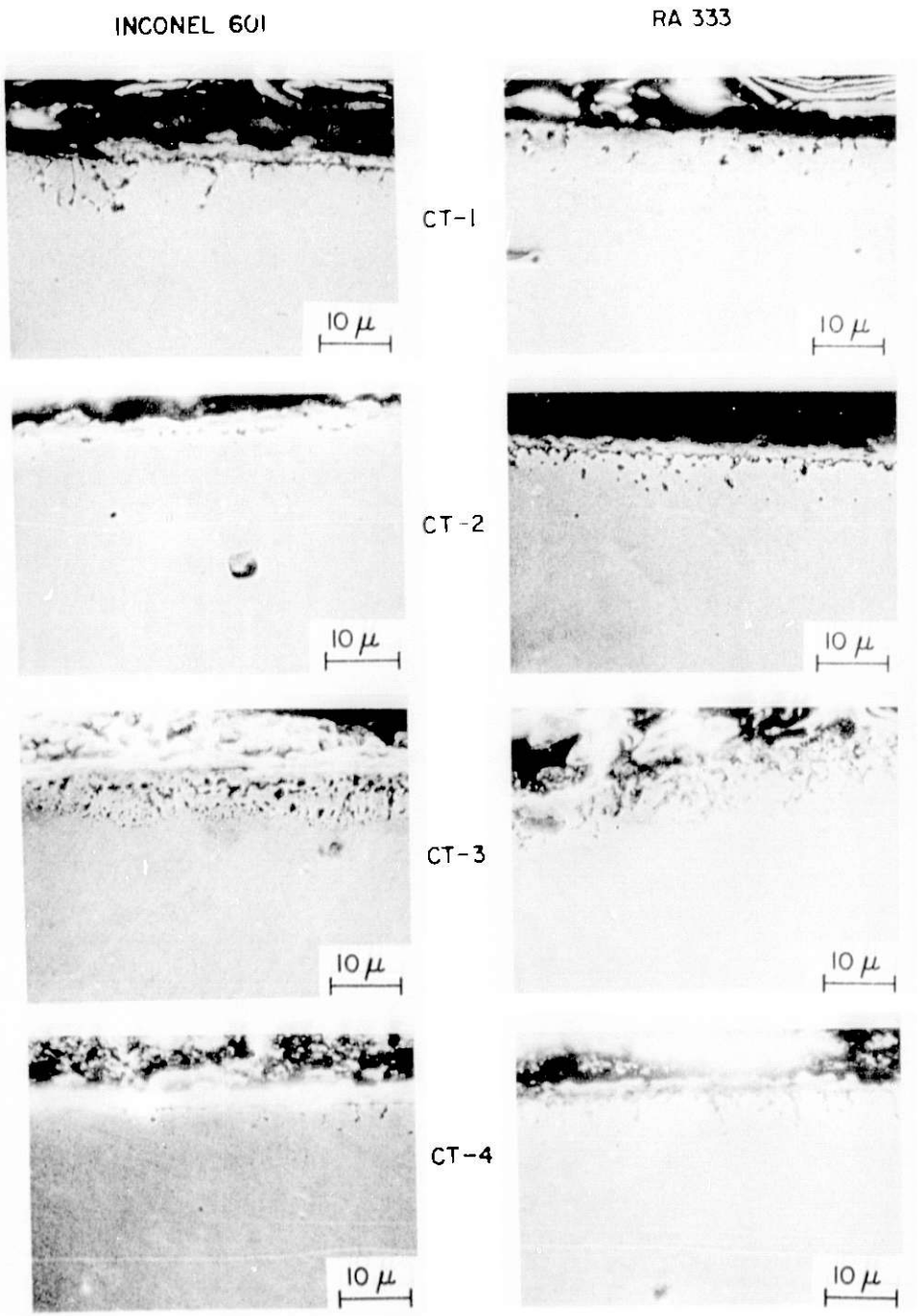

Fig. 25. SEM Micrographs of Inconel 601 and RA333 After a 100-h Exposure Inside the Fluidized Bed. CT-1, without salt; CT-2, 0.3 mol % $CaCl_2$; CT-3, 0.5 mol % NaCl; and CT-4, 1.9 mol % Na_2CO_3. ANL Neg. No. 306-79-682.

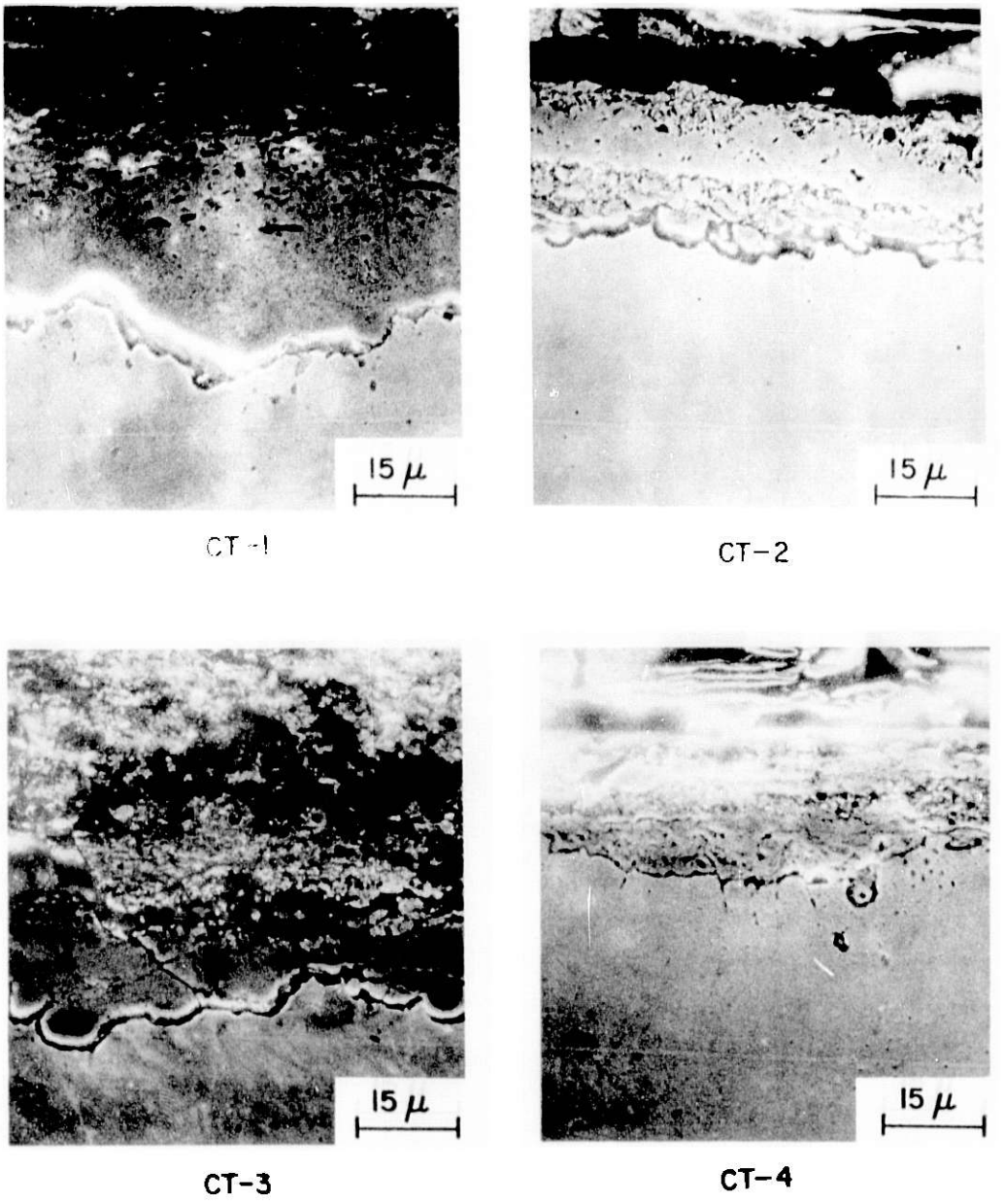

CT-1 CT-2

CT-3 CT-4

Fig. 27. SEM Micrographs of Fe-9Cr-1Mo Steel After a 100-h Exposure Inside the Fluidized Bed. CT-1, without salt; CT-2, 0.3 Mol % $CaCl_2$; CT-3, 0.5 mol % NaCl; and CT-4, 1.9 mol % Na_2CO_3. ANL Neg. No. 306-79-684.

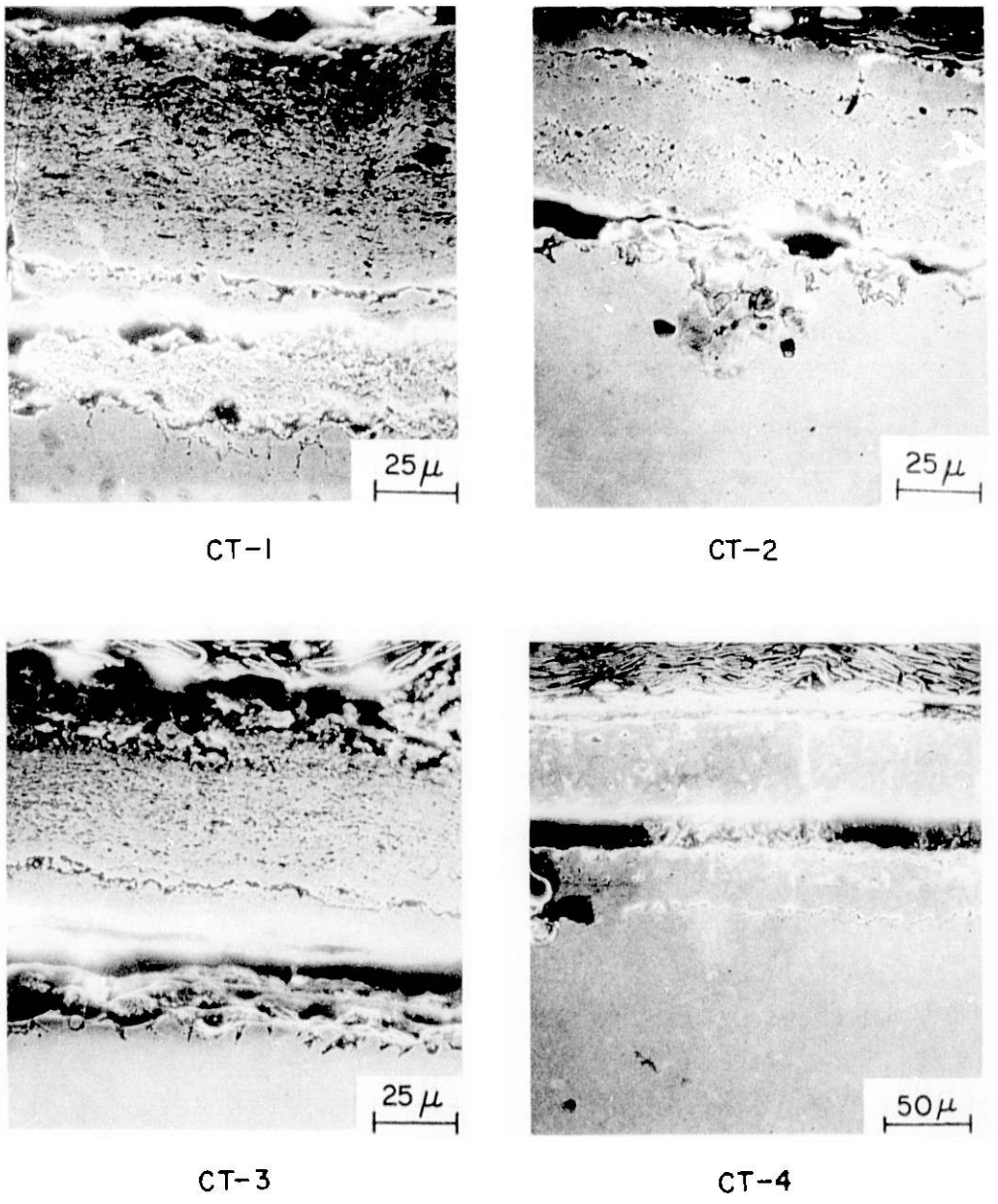

Fig. 26. SEM Micrographs of Fe-2-1/4Cr-1Mo Steel After a 100-h Exposure Inside the Fluidized Bed. CT-1, without salt; CT-2, 0.3 mol % $CaCl_2$; CT-3, 0.5 mol % NaCl; and CT-4, 1.9 mol % Na_2CO_3. ANL Neg. No. 306-79-683.

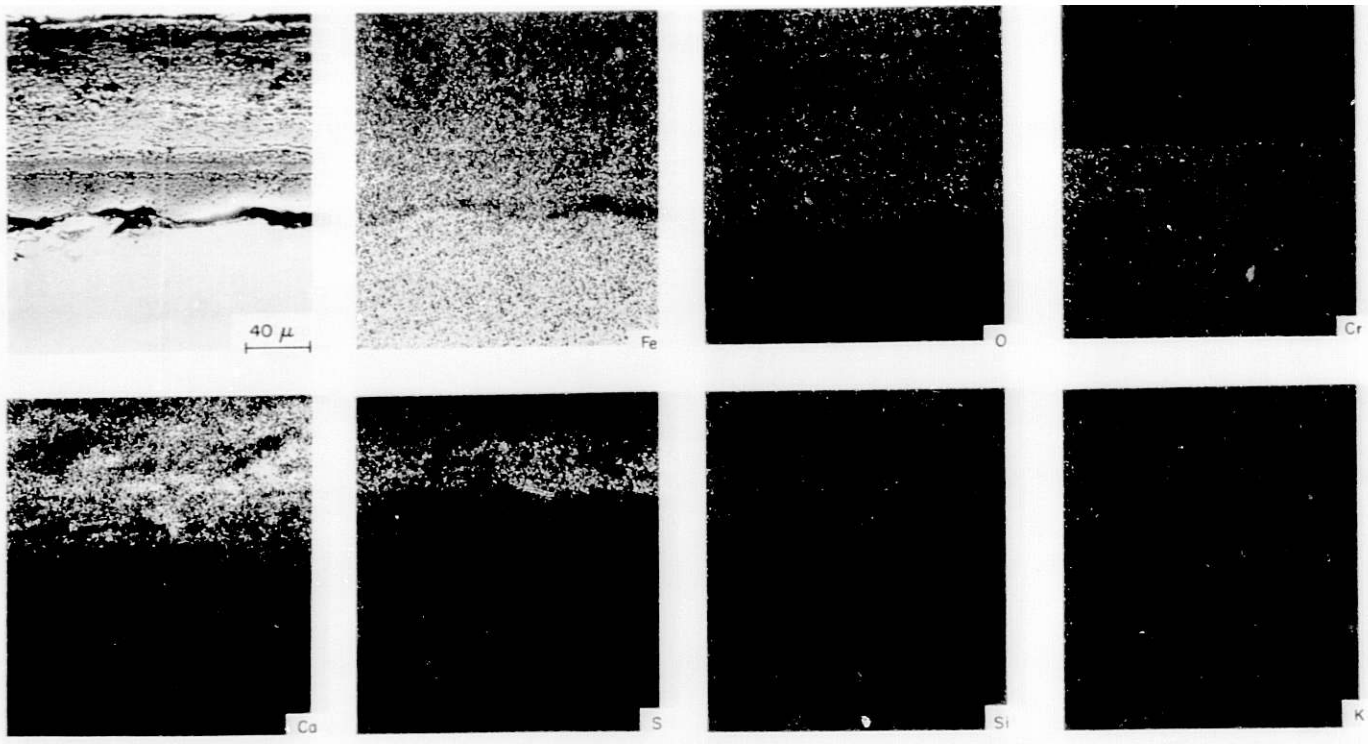

(a)

Fig. 28. SEM Micrograph and X-ray Images for Fe, O, Cr, Ca, S, Si, and K from a Fe-2-1/4Cr-1Mo Steel Specimen Exposed for (a) 100 h at 925 K Inside the Fluidized Bed, ANL Neg. No. 306-79-685 and (b) 100 h at 873 K Inside the Fluidized Bed Containing 0.5 mol % NaCl, ANL Neg. No. 306-79-686.

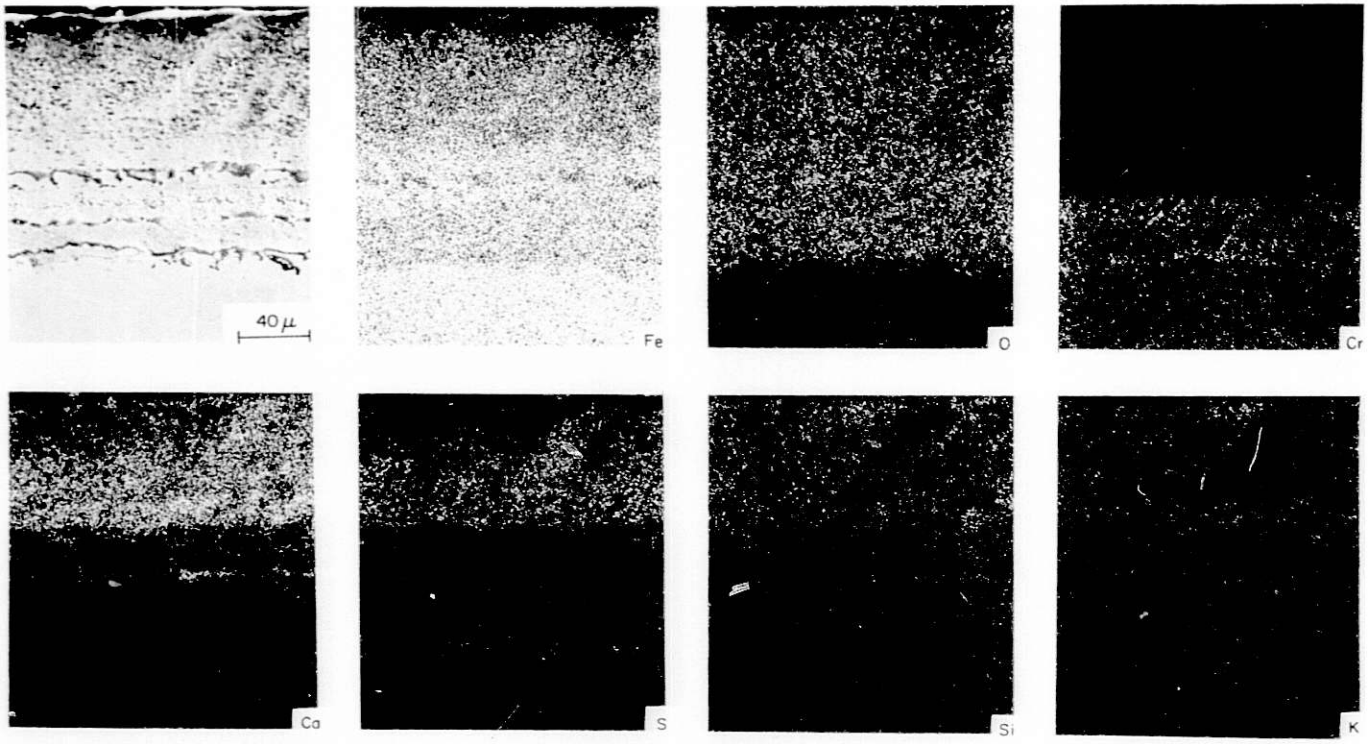

(b)

Fig. 28 (contd.)

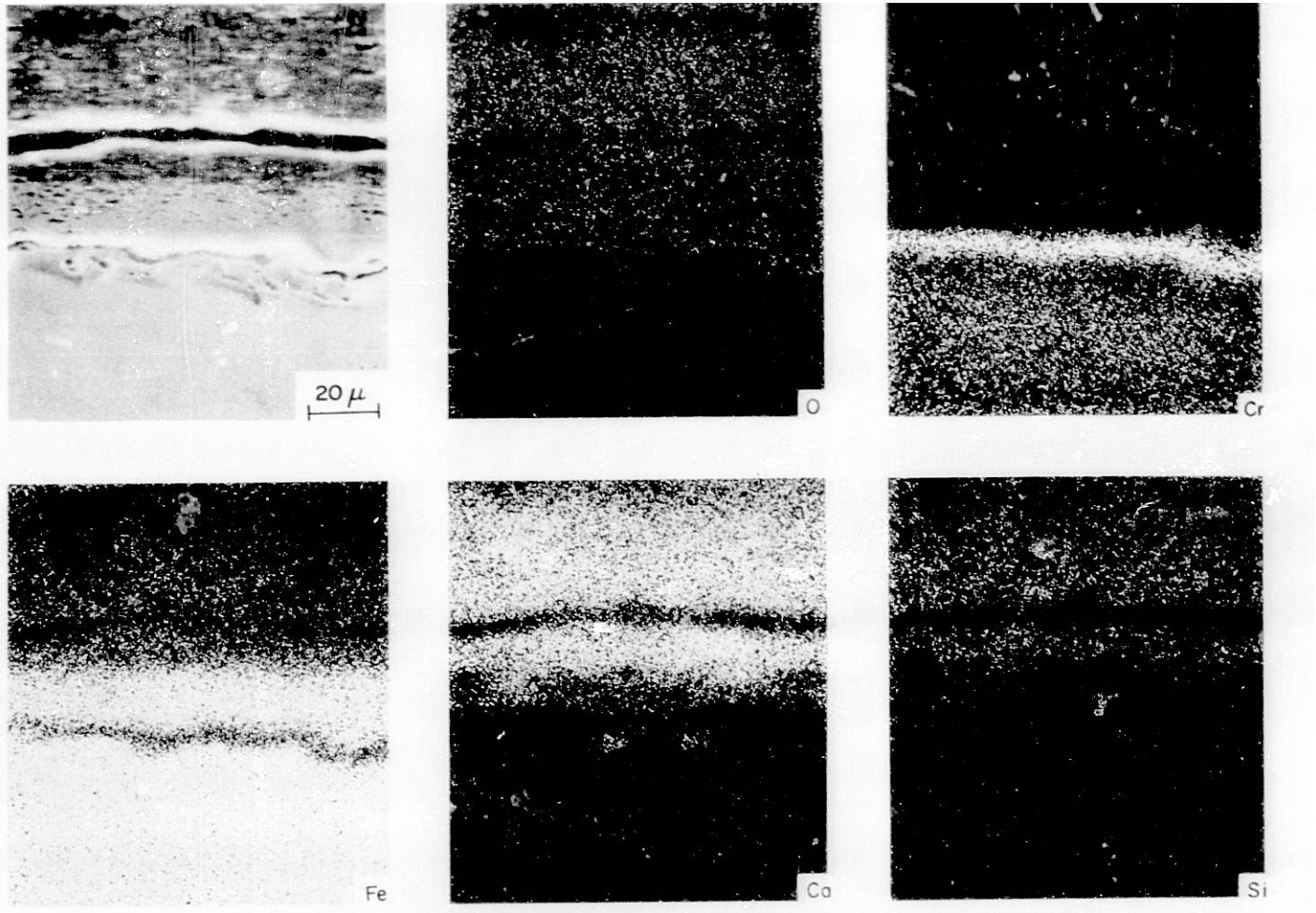

Fig. 29. SEM Micrograph and X-ray Images for O, Cr, Fe, Ca, and Si from a Fe-9Cr-1Mo Steel Specimen Exposed for (a) 100 h at 970 K Inside the Fluidized Bed, ANL Neg. No. 306-79-687 and (b)100 h at 895 K Inside the Fluidized Bed Contianing 0.5 mol % NaCl, ANL Neg. No. 306-79-688.

(b)

Fig. 29 (contd.)

Task E -- Erosion Behavior of Materials in Coal-conversion Processes
(J.Y. Park, S. Danyluk and W.J. Shack)

The objectives of the erosion program at ANL are to develop an engineering data base and the necessary analytical tools for rational design of components subject to erosive wear in coal-conversion plants. Engineering design data on erosive wear will be obtained from laboratory erosion testing which will be performed at temperatures and in atmospheres designed to simulate actual plant conditions. The laboratory results will be benchmarked against in-situ field measurements currently being obtained from the NDT program at ANL.

During the present quarter, a 150-h corrosion calibration test was performed on Stellite 6B, Type 304 SS, 1015 Carbon Steel and Incoloy 800 in a simulated gasifier atmosphere (CO 18, CO_2 12, CH_4 5, H_2 24, H_2O 39, NH_3 1, H_2S 1 in vol %) at 816°C. The equilibrium oxidation potential, sulfur potential, and carbon activity of this atmosphere are calculated to be 5.4×10^{-19}, 3.5×10^{-7} and 0.0214, respectively. Cross sections of specimens, examined after the test by optical metallography, are shown in Fig. 30. Significant amounts of corrosion occurred in all specimens. Material degradation due to corrosion was measured in terms of weight change, loss of substrate thickness, scale formation, and internal corrosion, as shown in Table XI. Carbon steel showed the greatest weight change, substrate loss, and scale formation. The corrosion scale of the carbon steel specimens contained many cracks (Fig. 30). Cracks were also observed at the interface between the scale and the metal substrate; these may result in the exfoliation of the scale and influence the long-term corrosion-rate measurement. Internal corrosion was not apparent in the carbon steel, but occurred in the other alloys under the scale near the substrate surface (Fig. 22). Stellite 6B, which had been expected to give the best performance among the alloys tested, showed significant weight change, substrate loss and internal corrosion. Incoloy 800 showed the least weight change, substrate loss, and scale formation. X-ray analyses of specimens are planned to examine the composition of the corrosion scales.

During the next quarter, a second corrosion calibration will be performed under the same test conditions in order to check the reproducibility of the tests and the reliability of the test apparatus. A new DC motor and speed control will be installed and room-temperature erosion-calibration tests will be started.

TABLE XI. Corrosion Calibration Test[a] Results

Material	Weight Change (gm/cm^2)	Loss of Substrate Thickness (in.)	Scale Thickness (in.)	Penetration (in.)
1015 Carbon Steel	+ 0.253	0.059	32×10^{-3}	-
Incoloy 800	+ 0.001	0.002	0.1×10^{-3}	0.5×10^{-3}
Type 304 SS	+ 0.024	0.002	0.5×10^{-3}	2×10^{-3}
Stellite 6B	+ 0.007	0.018	0.1×10^{-3}	4×10^{-3}

[a] 150 hours at 1500°F.

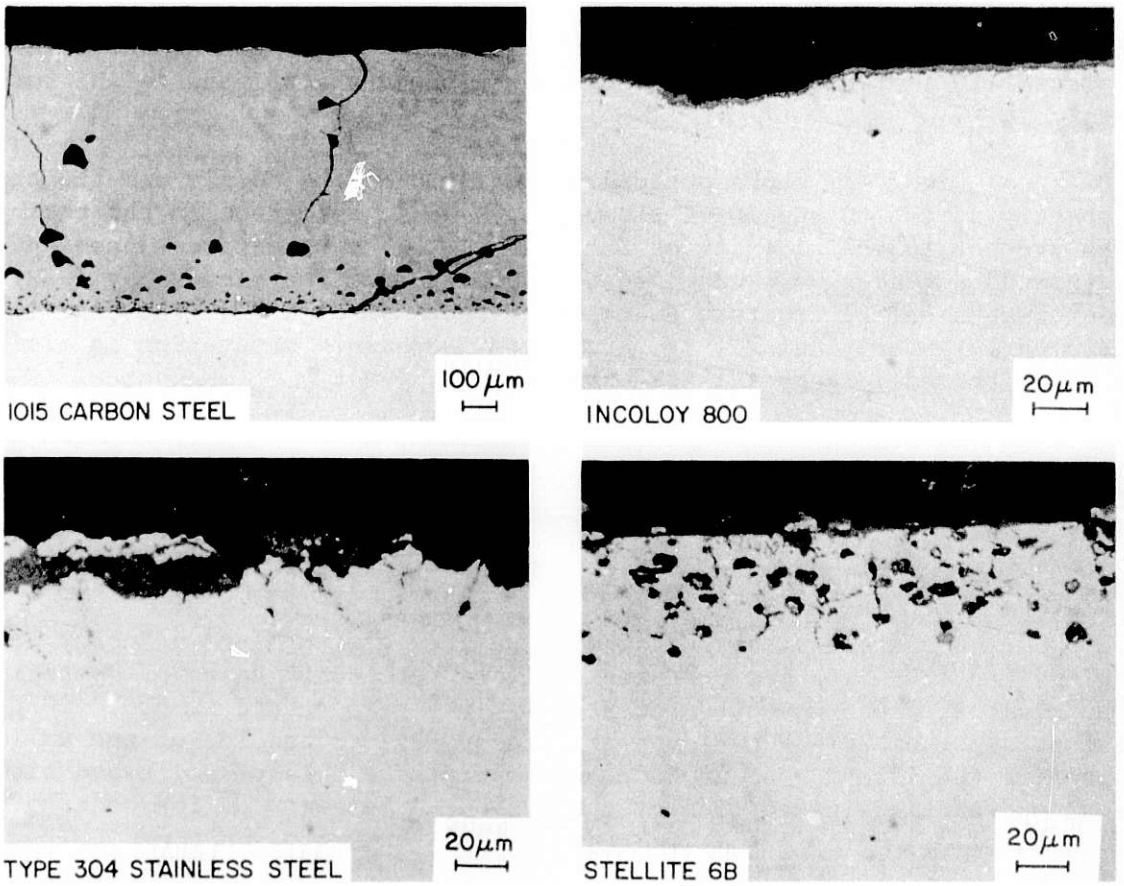

Fig. 30. Optical Micrographs of Cross Sections of Corroded Specimens Showing Corrosion Scale, Internal Corrosion and Metal Matrix.

Task F -- Component Performance and Failure Analysis *(S. Danyluk and G.M. Dragel)*

A cyclone nozzle failure from the Westinghouse Waltz-Mill Combined-Cycle Pilot Plant and an external cyclone failure from the Morgantown Energy Technology Center Stirred-bed Gasification Plant were examined during the present quarter. The results of these investigations are summarized below.

a. Westinghouse Waltz-Mill Cyclone Nozzle Failure

A crack was found in a connecting duct of a carbon steel (ASTM A106) nozzle that was welded to the external cyclone at the Westinghouse Waltz-Mill Pilot Plant. The nozzle was removed and shipped to ANL for analysis.

Figure 31 shows optical photographs of the nozzle and the crack geometry at the OD and ID of the pipe. A weld, not shown in the photographs, was present in the vicinity of the crack. The crack was sectioned and the separated surfaces were examined by scanning electron microscopy (SEM). SEM micrographs of the fracture surface are shown in Fig. 32. The cracking mode is clearly intergranular (Fig. 32a); grain-boundary separation is visible along with small recrystallized grains (Fig. 32b).

At present, the nozzle failure is attributed to intergranular stress-corrosion cracking. Additional data are being collected to substantiate these results.

b. Morgantown Energy Technology Center External Cyclone Failure

A Hastelloy X external cyclone from the Morgantown Energy Technology Center (METC) gas producer failed after twenty hours of operation. The cyclone, which was operated at a maximum temperature of 600°C (1200°F) and pressure of 7878 kPa (128 psig), failed by perforation of the wall opposite the inlet. The producer was operated with anthracite and bituminous coal and particle velocities at the cyclone inlet were of the order of 53 m/s (162 ft/s).

A schematic of the METC stirred-bed gasification system is shown in Fig. 33. Crushed coal is fed to coal-feed hoppers which in turn feed the gasifier. The producer gas is removed at the top and, after passage through the pressure letdown orifice, enters the cyclone (shown in detail in Fig. 34) where the ash fines are removed. The particulates and gas entering the cyclone are funneled and directed toward the back wall where the perforation occurred. Photographs of the sectioned cyclone, with the ID exposed, are shown in Fig. 35. Figure 35a shows the perforation; an edge view, including the back-plate weld overlay, is seen in Fig. 35b, and Fig. 35c shows a scalloped pattern observed on the ID along the entire length of the cyclone body, starting just below the inlet. A detailed examination of the ID revealed that the surface was plastically deformed by solid particles. Grooves formed by the impingement are evident in the SEM micrographs of Fig. 36. The grooves are essentially parallel and spaced $\sim$ 0.04 mm apart, with curled lips. Corrosion does not appear to have played a significant role in the failure.

In summary, the METC cyclone failure was due to solid-particle impingement, with corrosion apparently playing a minor role, if any. A replacement cyclone, made of Type 316 stainless steel, has been redesigned for particle velocities of ∿ 20 m/s (60 ft/s) and will be operated at lower temperatures.

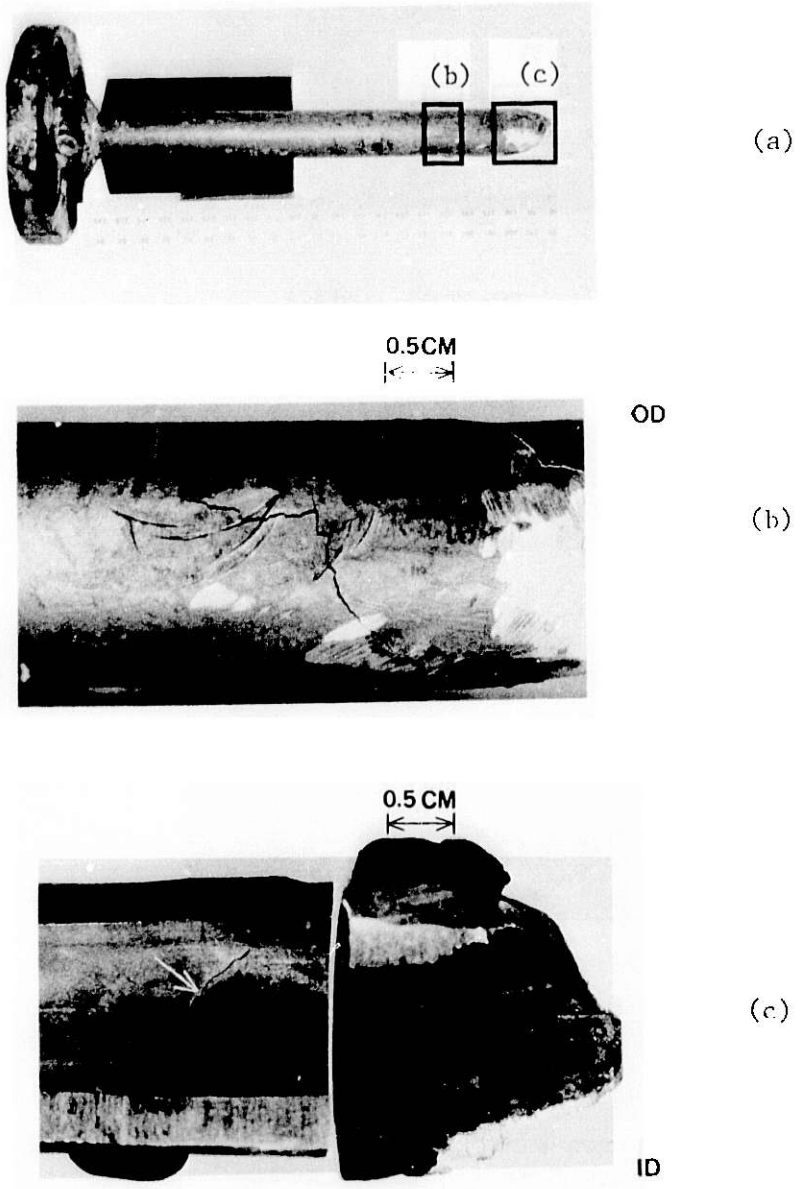

Fig. 31. Optical Photographs of the Failed Westinghouse Waltz-Mill Nozzle. (a) Overall view; (b) and (c) crack geometry at the OD and ID, respectively, of the regions indicated in (a). ANL Neg. No. 306-79-877.

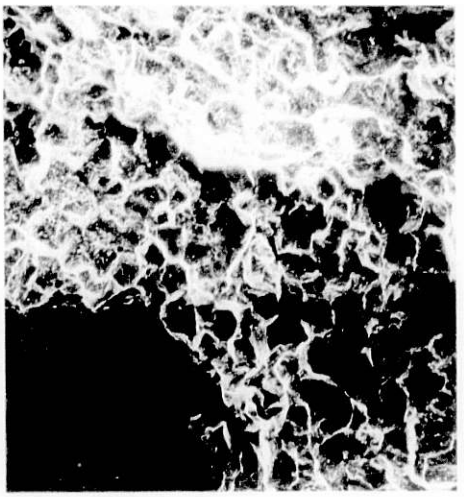

0.1 MM

(a)

(b)

Fig. 32. Scanning Electron Micrographs of a Fracture Surface from the Failed Nozzle, (a) away from and (b) near the OD. The crack shown by the arrow in Fig. 31c was sectioned and the crack surfaces separated. The fracture is intergranular. The grain size in the heat-affected zone is smaller than that of the base metal. ANL Neg. Nos. 306-79-875 and 878.

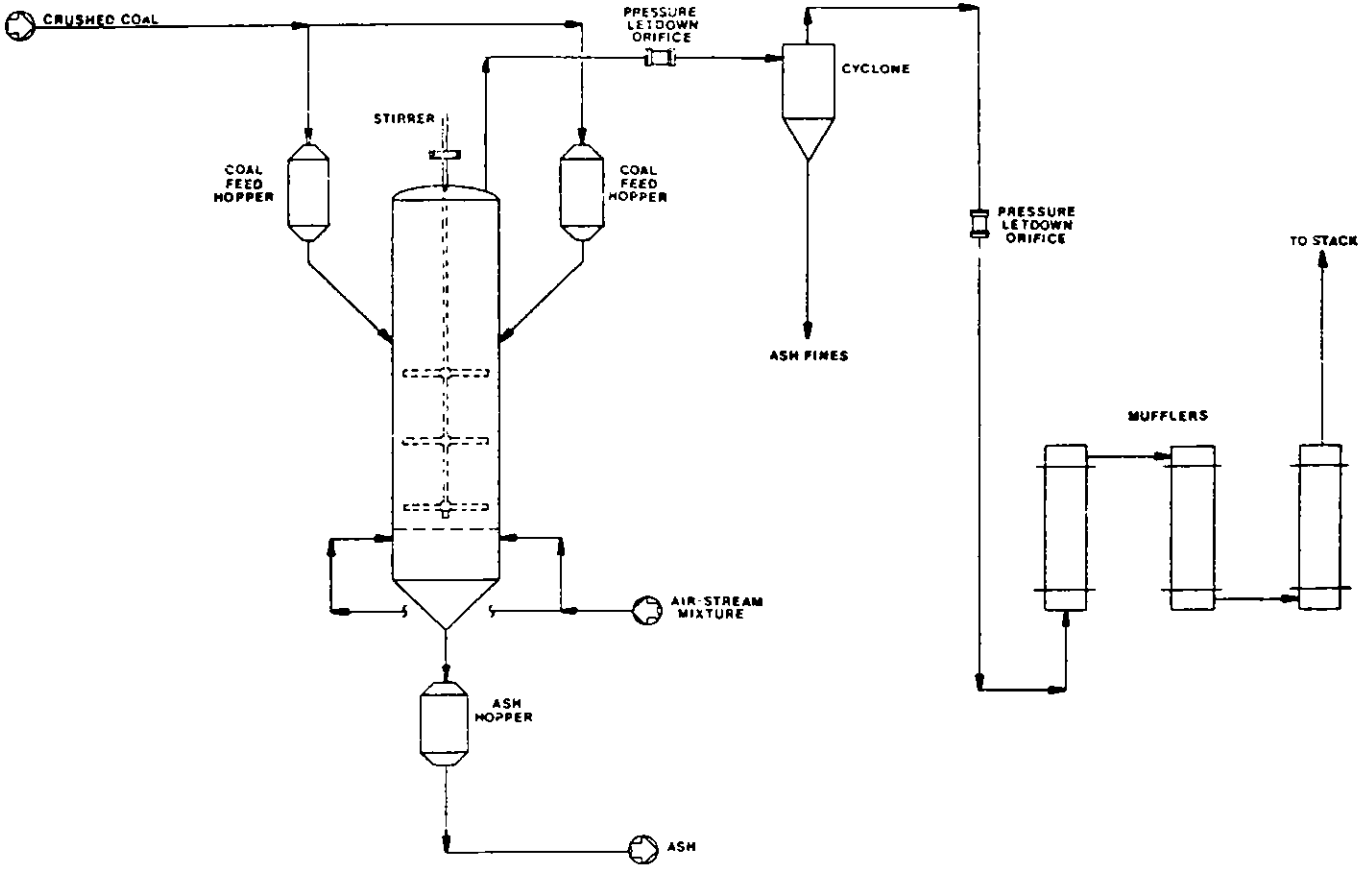

Fig. 33. Schematic Flow Diagram of Morgantown Energy Technology Center Stirred-bed Gasification System. ANL Neg. No. 306-79-867.

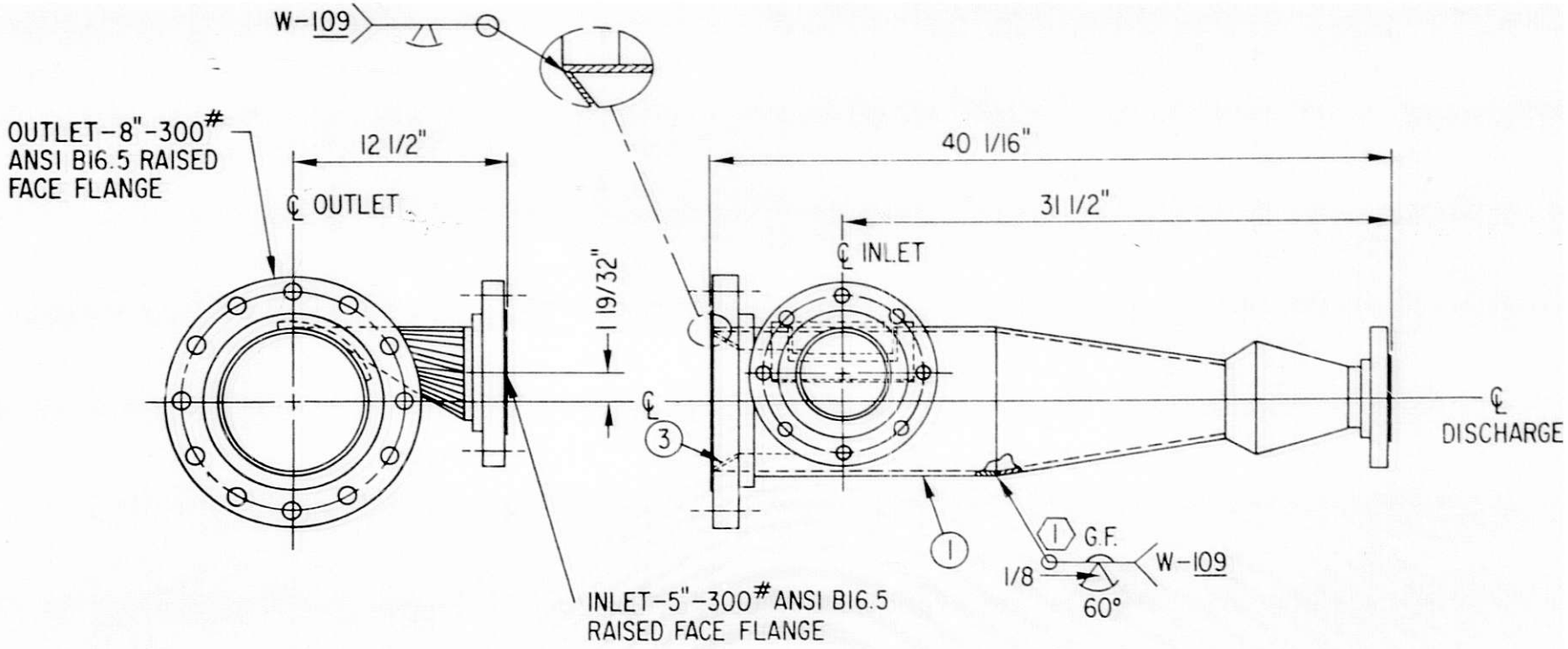

Fig. 34. Drawing of the METC Hastelloy X Cyclone. ANL Neg. No. 306-79-870.

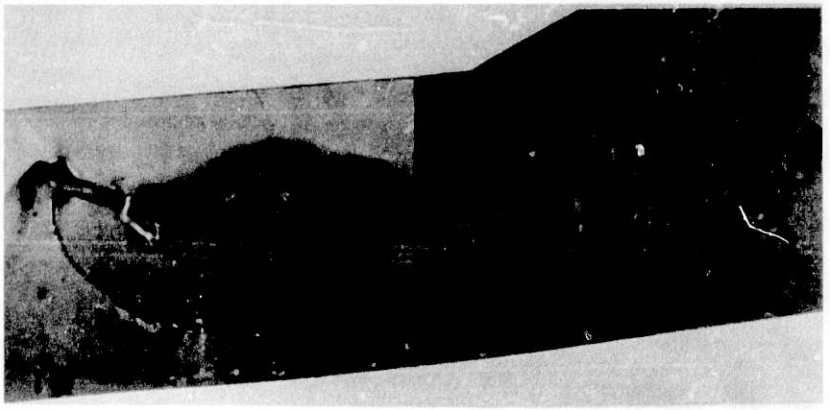

(a)

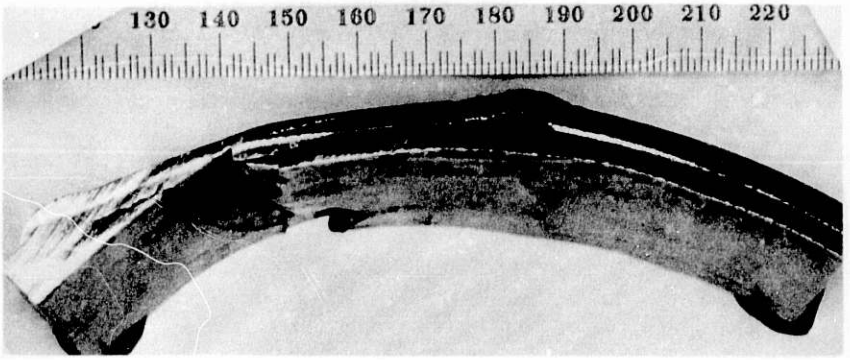

(b)

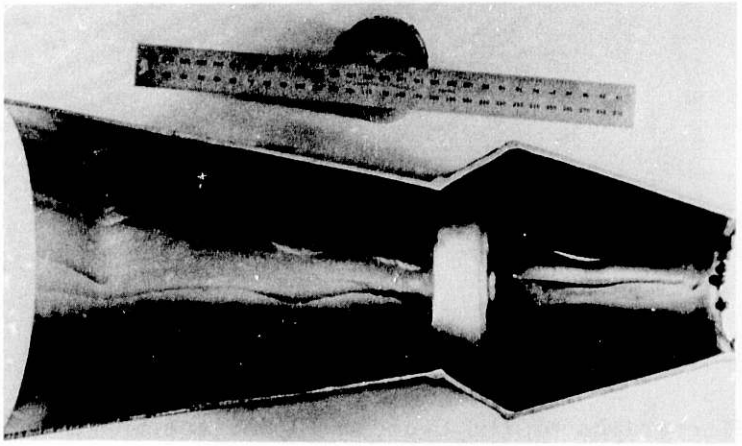

(c)

Fig. 35. Macrophotographs of METC Hastelloy X Cyclone. (a) ID surface, showing erosion and perforation pattern; (b) edge view of perforation with back-plate weld overlay; (c) ID surface, showing scalloped pattern extending the length of the cyclone from just below the inlet. ANL Neg. No. 306-79-934.

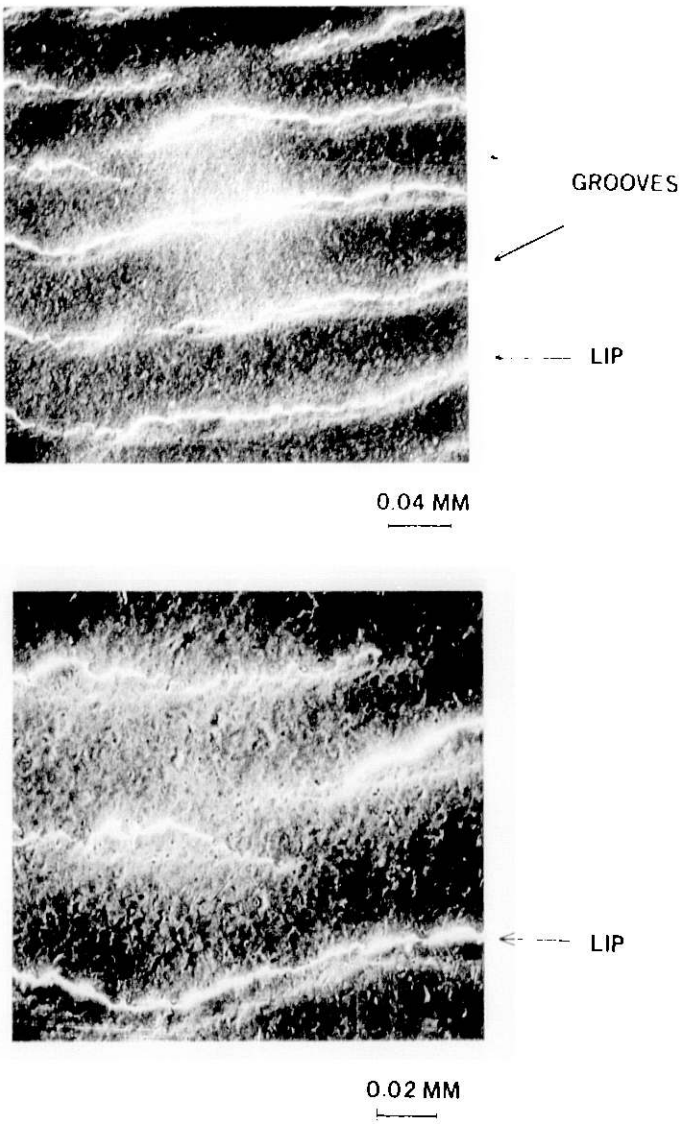

Fig. 36. SEM Micrographs of the Cyclone ID Surface Shown in Fig. 34. Solid-particle impingement has caused plastic deformation of the surface, with the formation of lipped grooves. ANL Neg. No. 306-79-876.

REFERENCES

1. Consultant Report from Dr. N. Fiore, University of Notre Dame to Argonne National Laboratory, dated April 16, 1979.

2. C.A. Youngdahl and W.A. Ellingson, "Long-term Erosion Monitoring of Metallic Conduits by Ultrasonic Pulse-echo Techniques," 12th Symposium on Nondestructive Evaluation, Southwest Research Institute, April 24-26, 1979. To be published in the Proceedings.

3. Foster, N.F., "Structure of CdS Evaporated Films in Relation to Their Use as Ultrasonic Transducers," J. Appl. Phys. 38 (1), 149-159 (1967).

4. Lord, A.E. Jr., "High-temperature Operation of Vacuum-evaporated, Thin-film Acoustic-wave Transducers," J. Appl. Phys. 37, 4593-4594 (1966).

5. L.C. Lynnworth and E.H. Carnevale, "Ultrasonic Testing of Solids at Elevated Temperatures," Proc. 5th Intl. Conference on NDT, Montreal, Canada, May 1967, The Queen's Printer, Ottawa (1967), pp. 303-307.

6. Private communication with N.O. Cross, EXXON Research and Engineering Company, Florham Park, NJ.

7. Private communication with Dr. R.O. Chaney, AMOCO Research Center, Naperville, IL.

8. J. and H. Krautkramer, Ultrasonic Testing of Materials, 2nd Edition, Translation of Third Revised German Edition, Springer-Verlag, New York (1977).

9. Karplus, H.B., "High-temperature Shear-mode Transducers for LMFBR Ultrasonic Flowmeters," Argonne National Laboratory Report, ANL-77-6 (Nov. 1976).

10. Materials Technology for Coal-conversion Processes, Seventeenth Quarterly Report, January-March 1979, Argonne National Laboratory, ANL-79-56.

11. Materials Science Division Coal Technology Ninth Quarterly Report, October-December 1976, Argonne National Laboratory, ANL-77-5.

12. Materials Technology for Coal-conversion Processes, Thirteenth Quarterly Report, January-March 1978, Argonne National Laboratory, ANL-78-54.

13. Materials Technology for Coal-conversion Processes, Fourteenth Quarterly Report, April-June 1978, Argonne National Laboratory, ANL-78-79.

14. K. Natesan, "Corrosion of Metals in Coal-gasification Environments," Proc. Conference on Corrosion/Erosion of Coal Conversion System Materials, ed. Alan V. Levy, National Association of Corrosion Engineers, Houston, TX (1979), pp. 22?-270.

15. R. A. Perkins and M. S. Bhat, "Sulfidation-Resistant Alloy for Coal Gasification Service," Lockheed Palo Alto Research Laboratories, Palo Alto, CA, FE-2299-12 (June 1977).

16. G. N. Irving, J. Stringer, and D. P. Whittle, Oxid. Met. 8, 393 (1974).

17. J. Podhorodeski, J. C. Colson, M. Lambertin, F. Nowack, and J. Kaczon, Proc. Conf. on Metal-Slag-Gas Reactions and Processes, ed. Z. A. Foroulis and W. W. Smeltzer, Electrochemical Society (1975), p. 437.

18. R. W. Bradshaw, R. E. Stoltz, and D. R. Adolphson, "Formation of Protective Layers on Alloys Used in Coal Gasification Environments," Sandia Laboratory Energy Report, SAND 77-8277 (November 1977).

19. V. L. Hill and B. A. Humphreys, "A Program to Discover Materials Suitable for Service Under Hostile Conditions Obtained in Equipment for the Gasification of Coal and Other Solid Fuels," Metals Properties Council Report, FE-1784-45, ed. A. O. Schaefer (November 1978).

20. K. Natesan, "Corrosion Problems in Coal-conversion Processes," Proc. Conf. on Scientific Problems of Coal Utilization, Morgantown, WV, ed. B.R. Cooper, DOE Symposium Series 46 (1978), p. 146.

21. Materials Technology for Coal-conversion Processes, Sixteenth Quarterly Report, October-December 1978, Argonne National Laboratory, ANL-79-23.